

Evaluating Wall Shear Stress Indices to Uncover Stimuli for Restenosis and Malapposition in Stented Coronary Arteries

Ali A. Aleiou
Marquette University

Recommended Citation

Aleiou, Ali A., "Evaluating Wall Shear Stress Indices to Uncover Stimuli for Restenosis and Malapposition in Stented Coronary Arteries" (2017). *Master's Theses (2009 -)*. 432.
http://epublications.marquette.edu/theses_open/432

EVALUATING WALL SHEAR STRESS INDICES TO UNCOVER
STIMULI FOR RESTENOSIS AND MALAPPOSITION
IN STENTED CORONARY ARTERIES

by

Ali A. Aleiou

A Thesis submitted to the Faculty of the Graduate School,
Marquette University,
in Partial Fulfillment of the Requirements for
the Degree of Master of Science

Milwaukee, Wisconsin

August 2017

ABSTRACT

EVALUATING WALL SHEAR STRESS INDICES TO UNCOVER STIMULI FOR RESTENOSIS AND MALAPPOSITION IN STENTED CORONARY ARTERIES

Ali A. Aleiou

Marquette University, 2017

The cause of coronary artery neointimal thickening leading to restenosis in ~10% of drug-eluting stents is unknown. Although research suggests adverse values of traditional wall shear stress (WSS) indices may contribute, studies to date have not accounted for stent geometry, which dictates local WSS patterns influencing drug concentration. Recently proposed WSS indices such as WSS variability and WSS exposure time (WSSET) may shed further light on restenosis or, the opposite effect, resorption. The objective of this investigation was to locally evaluate traditional and recently proposed post-stenting metrics and their respective impact on restenosis or resorption.

This study used de-identified data from 29 patients, randomized to thin-strut Promus Element, thin-strut Xience Prime, or thick-strut Nobori stents. All patients underwent optical coherence (OCT) and coronary computed tomography (CT) angiography post-stenting as well as at a 9-month follow-up. WSS metrics were calculated from computational fluid dynamics simulations of patient-specific 3D arteries, reconstructed by the fusion of OCT and CT angiography data, and normalized to WSS in the proximal unstented region. The change in lumen area (CLA) from post-stenting to follow-up was calculated using co-registered OCT pairs (469 pairs), corresponding to OCT imaging locations. The WSS results were compared with CLA using two-step cluster analysis.

Results showed that low WSS is a precursor to neointimal thickening, resulting in restenosis, confirming previous research. The Nobori stent was most prominent in the cluster with low WSS, potentially induced by the large radial thickness of the Nobori stent. Furthermore, high WSSET showed a relationship to restenosis. The combination of TAWSS combined with post-stenting WSS variability was shown to be directly related to CLA, which characterized vessel resorption. When vessel resorption occurs, regions of malapposition, uncovered struts or malapposed struts may develop. These are undesirable features, which potentially result in late stent thrombosis. In all, the results from this collection of multiple local analyses provide insight into potential predictive indices of local artery restenosis and resorption after stenting. If confirmed through future prospective studies, these indices may improve the efficacy of drug-eluting stents, thereby improving the quality of life for patients with coronary artery disease.

ACKNOWLEDGMENTS

Ali A. Aleiou

First and foremost, I am sincerely grateful for the opportunity my advisor Dr. John LaDisa has given me. From the moment I met with him in the fall of 2012, I knew that his passion and charisma towards research was something I admired and was what I needed to develop in biomedical engineering. The opportunity to work on many avenues of cardiovascular research with him has been priceless and will, no doubt be of utmost importance in my professional development moving forward.

Second, I would like to acknowledge the continuous support from Dr. Laura Ellwein, Dr. Kristina Ropella, and Dr. Mehdi Maadooliat, who not only served on my committee, but were always there to provide guidance. I also would like to thank Dr. Hiro Otake, Dr. Shawn Shadden, and Dr. Amirhossein Arzani for their valuable collaboration in this project. Their time and efforts are greatly appreciated. The constant support and advice from these distinguished scholars has truly been inspirational and critical to the success of this project, and to me personally as a biomedical researcher and graduate student. I am forever grateful for their time and efforts.

Most important, I would like to show thanks towards my family. To my mother, Sandra Whitehead, for always being there for me and encouraging me. Her love is my motivation and I am lucky to have such a wonderful in person my life. To my Baba, Aziz Aleiou, for always being the rock of the family. His life of genuine sincerity and appreciation towards others is something I love him for and aspire to emulate in my life. To my siblings, Aisha and Adam, for your love and encouragement. I could not be the brother I am today without having such awesome siblings and instant friends.

Finally, I would like to thank the Marquette Biomedical Engineering community, students, faculty and staff. Dr. Scott Beardsley guided and supported me in my role as the Head Biomedical Teaching Assistant. Dr. Taly Gilat-Schmidt has also always encouraged, motivating me to be the best biomedical engineer I can be. In addition, I am grateful for my friends, the biomedical engineering graduate students that I have met, will also be forever remembered. I have made lifelong friends and know that we all will be moving on to do great things in the field.

Special thanks go to Dr. Said Audi for his continuous support and encouragement in my professional and personal life. Dr. Audi has been in my life since I was a baby. I am grateful for the positive influence he has had on me throughout.

TABLE OF CONTENTS

ACKNOWLEDGEMENTS	i
LIST OF ACRONYMS	v
CHAPTER 1: INTRODUCTION	1
1.1 Cardiovascular Disease	1
1.2 Evolution of Treatment Methods for Coronary Stenoses	3
1.3 Restenosis and Resorption from Stenting	6
1.4 Restenosis and Stent Geometry Causing Blood Flow Alterations.....	10
1.5 Methods for Quantifying Intravascular Efficacy and Hemodynamic Impact of Stents.....	12
<i>1.5.1 Intravascular Ultrasound.....</i>	<i>12</i>
<i>1.5.2 Optical Coherence Tomography.....</i>	<i>12</i>
<i>1.5.3 Computational Fluid Dynamics.....</i>	<i>13</i>
1.6 Hemodynamic Indices	14
1.7 Objective and Specific Aims	17
<i>Specific Aim 1: Evaluate the ability of traditional and recent WSS indices locally to predict neointimal thickening, or conversely, arterial resorption after drug-eluting stent implantation</i>	<i>17</i>
<i>Specific Aim 2: Use cluster analysis to uncover which stent design and/or patient-specific attributes correlate with neointimal thickening or vessel resorption using complex drug-eluting stent datasets containing traditional and recent WSS indices.....</i>	<i>18</i>
CHAPTER 2: METHODS.....	19
2.1 Preprocessing	19
2.1.1 Data Acquisition	19

2.1.2 Patient-Specific Vessel Reconstruction.....	21
i. Image Processing.....	21
ii. Wire Pathway Reconstruction	22
iii. Segment Registration.....	23
iv. Model Assembly	24
2.1.3 Computational Stent Implantation.....	27
2.1.4 Stented Model Accuracy Checks	32
2.1.5 Simulations.....	34
i. Meshing.....	34
ii. Boundary Conditions	36
iii. Governing Equations.....	39
2.1.6 Post-Processing	40
i. Data Normalization	40
ii. Local Analyses	41
iii. Isolation of Vessel Wall Indices.....	42
iv. Normalized TAWSS Variability.....	43
v. Wall Shear Stress Exposure Time	46
vi. Local Change in Lumen Area between Post and Follow-Up OCT Pairs	47
vii. Average of Post-Stenting Metrics	49
viii. Cluster Analysis and Supplemental Marker Indices.....	49
CHAPTER 3: RESULTS.....	52
3.1 Aim 1: Local Analyses of a Case with Both Positive and Negative CLA.....	52
3.2 Local Analyses Ranges of Quantified Post-Stenting Metrics from Aim 1	58

3.2.1 <i>Local Analysis Example of Low vs High Normalized TAWSS</i>	58
3.2.2 <i>Local Analysis Example of Low vs High Normalized TAWSS Variability</i>	60
3.2.3 <i>Local Analysis Example of Low vs High Normalized WSSET</i>	61
3.3 Aim 2 Results: Two-Step Cluster Analysis for All Cases	63
3.3.1 <i>Collection of Patient-Specific Post-Stenting Results</i>	63
3.3.2 <i>Two-Step Cluster Analysis Summary</i>	64
3.3.3 <i>Two-Step Cluster Analysis Absolute and Relative Distributions</i>	65
3.3.4 <i>Two-Step Cluster Comparison of Three Output Clusters</i>	66
CHAPTER 4: DISCUSSION.....	68
4.1 Overview of Specific Aims and Summary of Major Findings	68
4.2 Review of Findings from Aim 1: Local Relationship of Traditional and Recent WSS Indices to NT and Vessel Resorption	70
4.3 Review of Findings from Aim 2: Cluster Analysis Significance	76
4.4 Limitations and Future Directions	80
BIBLIOGRAPHY.....	83

LIST OF ACRONYMS

(in order of appearance)

CVD = cardiovascular disease

CAD = coronary artery disease

PCI = percutaneous coronary intervention

POBA = plain old balloon angioplasty

BMS = bare-metal stent

ISR = in-stent restenosis

DES = drug-eluting stent

EC = endothelial cells

BVS = bioresorbable vascular scaffolds

NT = neointimal thickening

WSS = wall shear stress

TAWSS = time-averaged wall shear stress

CFD = computational fluid dynamics

IVUS = intravascular ultrasound

OCT = optical coherence tomography

OSI = oscillatory shear index

WSSET = wall shear stress exposure time

WSSG = wall shear stress gradient

CTA = computed tomography angiography

FEA = finite element analyses

CDASD = central difference approximation to the second derivative

CLA = percent change in lumen area

IA = intracranial aneurysms

Chapter 1

Introduction

1.1 Cardiovascular Disease

The most recent American Heart Association annual statistical update estimates that 85.6 million American adults (>1 in 3) have at least one type of cardiovascular disease (CVD) (Mozaffarian et al., 2016). In every year since 1900 except 1918, CVD accounted for more deaths than any other major cause of death in the United States (Mozaffarian et al., 2016). The most prevalent form of CVD is coronary artery disease (CAD). A study from 2013 showed CAD was solely responsible for ≈ 1 of every 7 deaths in the United States (Mozaffarian et al., 2016). CAD affects approximately 46% of those suffering from CVD and is the leading cause of death in the United States, killing more than 2,200 Americans a day, an average of 1 death every 40 seconds (Mozaffarian et al., 2016).

Three main coronary arteries (left anterior descending, left circumflex, and right coronary arteries) lie on the surface of the heart and branch into smaller coronary arteries, which penetrate the cardiac muscle mass (Guyton & Hall, 2006). The heart receives most of its nutritive blood supply through these coronary arteries (Guyton & Hall, 2006). An illustration of these coronary arteries can be seen in Figure 1.

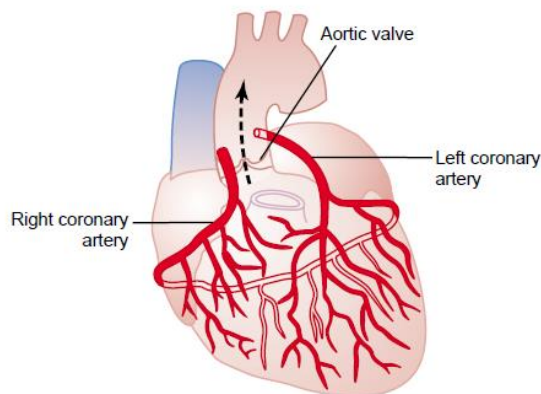


Figure 1: The coronary arteries (Guyton & Hall, 2006).

Atherosclerosis is triggered by chronic inflammation at the site of damaged vascular endothelium (inner lining of vessel wall) and lipid loaded foamy macrophages derived from infiltration of monocytes into the arterial wall (Komiyama et al., 2015). Atherosclerosis is primarily an endothelial disease of large and medium-sized arteries, and most commonly has the effect of causing arterial narrowing (or stenosis) and reduction of blood flow to the tissues (Nichols, O'Rourke, & Vlachopoulos, 2011). Libby et al schematically described the process of atherosclerosis through a series of steps leading to arterial stenosis, shown in Figure 2 (Nichols et al., 2011).

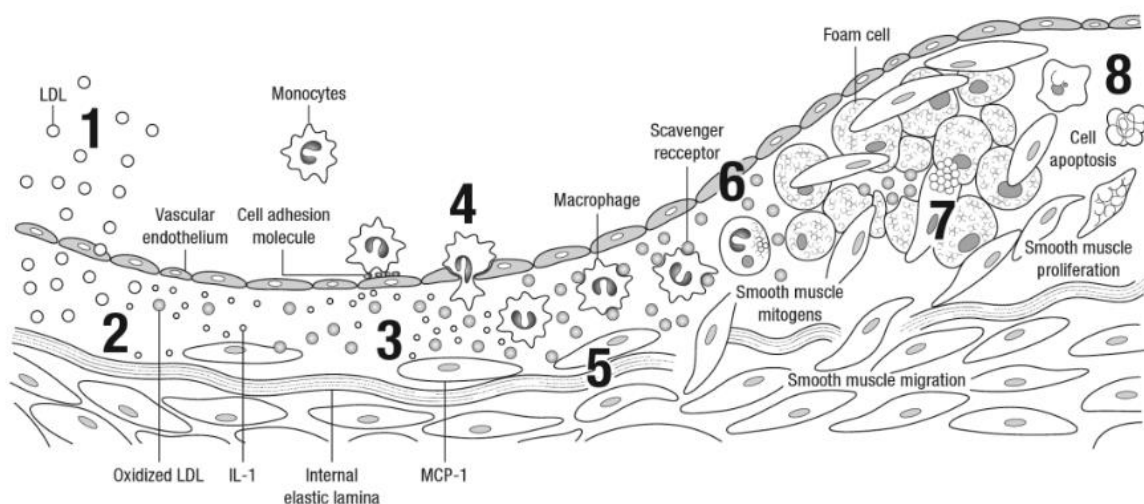


Figure 2: Schematic of the evolution of atherosclerosis as described by Libby (Nichols et al., 2011).

Stenoses that occur in any of the three coronary arteries may be associated with myocardial infarction, or heart attack, which may ultimately result in ischemia and cell death in the region of restricted blood flow. Therefore, percutaneous coronary intervention (PCI) was developed to address this problem. PCI is now accepted worldwide for the treatment of CAD due to atherosclerosis (Komiyama et al., 2015).

1.2 Evolution of Treatment Methods for Coronary Stenoses

One early type of PCI is referred to as Plain Old Balloon Angioplasty (POBA), which began with the first procedure occurring in 1977 to treat angina pectoris (i.e. chest pain resulting from myocardial ischemia). The first spring-loaded self-expandable stainless steel Wall stent (Medinvent SA, Lausanne, Switzerland) was implanted in the coronary tree in 1986 by Sigwart et al (Chopra & Nanda, 2013; Komiyama et al., 2015). In a 1994 randomized clinical trial, bare-metal stents (BMS) proved to be better than POBA in short-term procedural success and long-term arterial patency, however in-stent restenosis (ISR) occurred in 20-30% of the cases, ultimately leading to PCI failure for those cases (Komiyama et al., 2015). (The term “case” refers to a single stented lesion in the coronary tree. A patient in this study may have multiple cases.) This re-closing of the vessel in the stented region became known as the “Achilles’ heel” of balloon angioplasty (Komiyama et al., 2015). ISR may be severe enough to require repeat revascularization, which is a procedure to re-open the affected coronary artery by either deploying another stent in the stenosed artery or undergoing a bypass operation.

With ISR remaining a prevalent issue with stenting, further advancements in stent technology were pursued. The subsequent development and application of drug-eluting stents (DES), which involve the controlled local release of antiproliferative agents to combat ISR (Stefanini & Holmes, 2013), have been shown to reduce the risk of repeat revascularization, as compared with BMS in many cases (Bønaa et al., 2016; Stettler et al., 2007). In contrast to BMS, early DES consisted of three components: (1) a metallic stent platform, (2) a polymer coating, and (3) an antiproliferative agent (Stefanini & Holmes, 2013). The polymer coating was sometimes applied to the stent surface to serve as a drug carrier and permit controlled drug release (Stefanini & Holmes, 2013). These components are shown in Figure 3 below.

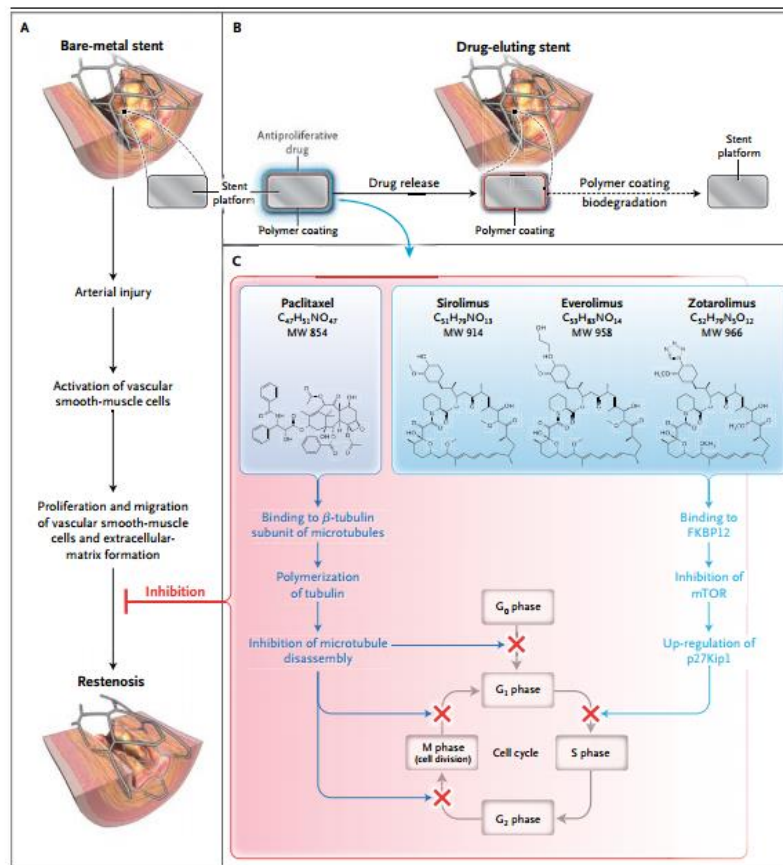


Figure 3: Bare-metal stent vs. drug-eluting stent (A) Bare-metal stent leading to restenosis; (B) Drug-eluting stent platform, polymer coating and antiproliferative drug layering; (C) Inhibitory antiproliferative drug action on cell cycle.

One current version of a DES has since replaced the metallic stent platform, which enables the radial strength of the stent to hold the artery open, with a durable polymer and omits the need for the polymer coating used in early DES (Parsa et al., 2016).

Current-generation antiproliferative agents are composed of highly lipophilic molecules that are distributed into the arterial wall via the stent, and exert either immunosuppressive effects or antiproliferative effects preferentially on smooth-muscle cells, while allowing for endothelial cells (EC) to reestablish themselves on the surface of the artery (Stefanini & Holmes, 2013). Understanding the specific attributes of the stent geometry as well as the drug-elution effects are important in determining of the effectiveness, or lack thereof, with DES. For example, Nakano et

al indicates that inadequate drug concentration due to wider inter-strut distance and vessel injury are primary mechanisms of DES restenosis and occlusion, respectively (Nakano et al., 2013).

Various antiproliferative agents on the surface of DES have been researched and were found to have different outcomes. For example, stents that release sirolimus or paclitaxel showed a marked reduction in the rate of repeat revascularization as compared to BMS, but have been associated with an increased risk of very late stent thrombosis as compared to BMS (Stefanini & Holmes, 2013). Everolimus-eluting stents showed improved clinical outcomes as compared with paclitaxel-eluting and sirolimus-eluting stents, reducing the risks of repeat revascularization, myocardial infarction, and stent thrombosis (Stefanini & Holmes, 2013). Therefore, drug-elution behavior can be analyzed with respect to its independent action on the endothelial and medial layers of the vessel, which should be considered when analyzing DES.

Bioresorbable vascular scaffolds (BVS) offer a promising new technology that may be the way of the future in treating ISR. BVS have been dubbed the “fourth revolution” in interventional cardiology, showing the ability to treat the coronary lesion and restore endothelial function after complete absorption (Wayangankar & Ellis, 2015). This novel advancement in interventional cardiology is intuitive in that physicians and patients would agree that a stent which disappears after its useful function is achieved would be a superior device to a permanent metallic implant (Byrne & Kastrati, 2015). Onuma et al began research of BVS in porcine coronary artery models and showed that, after two years, the struts are discernable by imaging and at three and four years, both imaging and histology confirm complete integration of the struts into the arterial wall (Onuma et al., 2010). This technology, while still in the early phases of clinical trials, shows promise in the possible impact it could have on the field of endovascular intervention (Byrne & Kastrati, 2015).

1.3 Restenosis and Resorption from Stenting

Following the implantation of a BMS (i.e. non-DES), the vessel may react one of two ways: the vessel may re-narrow (restenosis) or the vessel wall may atrophy away from the stent (resorption). Angiographic restenosis is defined as a loss of greater than 50% of the initial arterial diameter gained from the stenting procedure (Murphy & Boyle, 2010). Restenosis is reported to occur through four main mechanisms: (1) thrombosis, (2) arterial inflammation, (3) neointimal thickening (NT), and (4) remodeling (Murphy & Boyle, 2010). Target-lesion revascularization is a repeat revascularization procedure of the initial stenotic lesion when restenosis of >50% occurs within the stented region and results in a positive stress test (Lee et al., 2015). A stress test, also called a treadmill or exercise test, is used by physicians to determine how well the patient's heart can handle physical activity.

Following the implantation of a coronary stent, the initial reaction of the vessel wall is thrombosis (Murphy & Boyle, 2010). Arterial injury occurs by damage to the inner artery wall, plaque compression and, in extreme situations, dissection of the inner arterial wall (Murphy & Boyle, 2010). This injury of the artery by the stent during the deployment process causes the attraction of blood-borne platelets to the source of arterial injury around the stent struts, which adhere to the damaged cells and release chemical attractants for other platelets (Murphy & Boyle, 2010). A protein called fibrin then forms around the platelets to bind them together into a thrombus, which is the dominant physiological response in the first seven days after implantation (Murphy & Boyle, 2010). Early studies had a difficult time accurately defining stent thrombosis, making comparisons across reports challenging (Stefanini & Holmes, 2013). The Academic Research Consortium subsequently provided standardized criteria for the definition of stent thrombosis based on the time of occurrence (i.e., early, ≤ 1 month; late, >1 month to ≤ 1 year; or very late, >1 year) (Stefanini & Holmes, 2013). While the occurrence of stent thrombosis following DES deployment remain incompletely understood, it is likely that hampered or delayed

vascular re-endothelialization is centrally involved (Seo, Lafont, Choi, & Barakat, 2016). This exposure of stent struts directly to blood flow for longer periods of time increases the likelihood of in-stent thrombotic events (Seo et al., 2016).

Arterial inflammation occurs when the immune system reacts to the presence of the stent (Murphy & Boyle, 2010). This inflammatory response occurs within 24 hours of stent implantation where white blood cells infiltrate the vessel wall around the site of the injury (Murphy & Boyle, 2010). White blood cells are transported via blood flow and are chemically attracted to the site of the injury, which is a similar behavior to the thrombotic events described above (Murphy & Boyle, 2010). White blood cells infiltrate the injured vessel wall at the site of the injury induced by the stent, and the collection of these cells in the arterial wall contribute to the local restenosis occurring due to the inflammatory response.

NT, the primary cause of restenosis, occurs within weeks after stent implantation to re-narrow the stented artery (Murphy & Boyle, 2010). If NT is minimal, the stenting procedure will be considered successful (Murphy & Boyle, 2010). Figure 4 shows two different examples showing minimal and significant NT. Specifically, NT is a process by which smooth muscle cells, which normally reside in the middle layer of the artery, migrate inwards towards the stent where they proliferate and form the bulk of the new tissue blocking the artery.

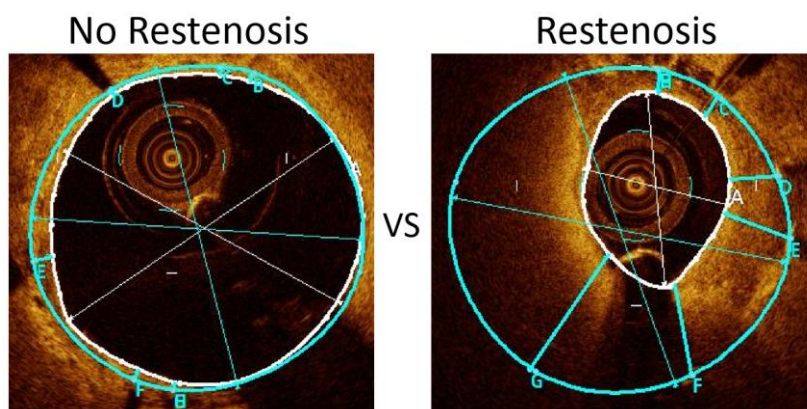


Figure 4: Optical coherence tomography images showing cross sections of a stented artery exhibiting restenosis at 9-month follow-up (right) and a stented artery without restenosis (left). Teal circles correspond with the stent location and white circles correspond with vessel wall locations.

The final cause of restenosis is remodeling. Approximately 4 week after stent implantation, collagen deposits in the outer layers of the artery lead to arterial shrinkage known as negative remodeling (Murphy & Boyle, 2010). Some researchers believe this “arterial shrinkage” process increases the pressure on the stent and can squeeze some of the artery wall through the inter-strut space from without (Murphy & Boyle, 2010). The artery wall protruding into the lumen space may then contribute to restenosis, blocking the artery.

Another outcome of stenting may be resorption, where arteries undergo delayed arterial healing, which may be associated with uncovered struts or if, severe enough, could result in malapposed struts. Figure 5 shows two different examples with resorption; without uncovered or malapposed struts and with both uncovered and malapposed struts. This enlargement of the lumen wall may be due to adaptive outward remodeling, where chronically elevated flow may induce an artery to undergo outward remodeling to restore the shear stress on the vessel wall back to baseline levels (Dolan, Kolega, & Meng, 2013). In theory this phenomenon may also be due to elevated concentration of the elution agents on DES, but this hypothesis has yet to be rigorously tested.

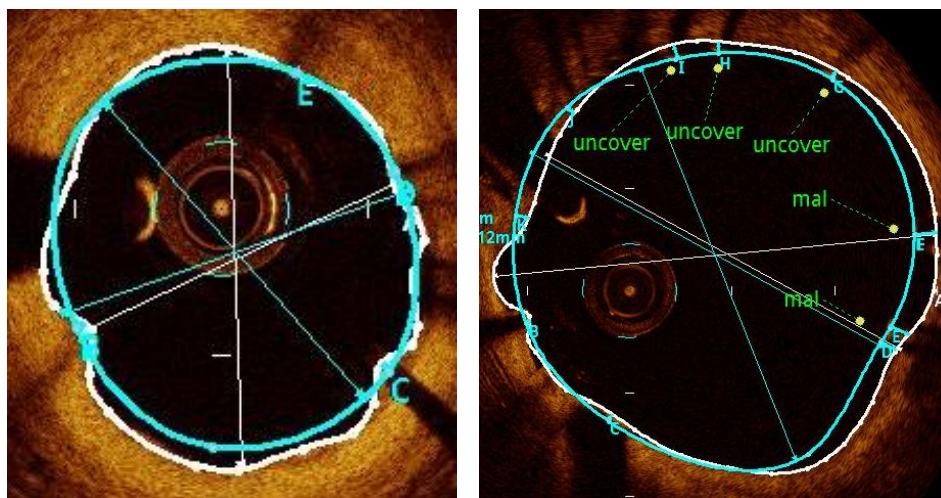


Figure 5: Optical coherence tomography images at 9-month follow-up show vessel resorption without marked uncovered or malapposed struts (left) and with both marked uncovered and malapposed struts (right).

The different reactions of the vessel following the implantation of a coronary stent, such as restenosis by NT and resorption by delayed arterial healing mentioned above, as well as physiological healing, can be seen schematically as A, B, and C respectively in Figure 6 (Stefanini & Holmes, 2013).

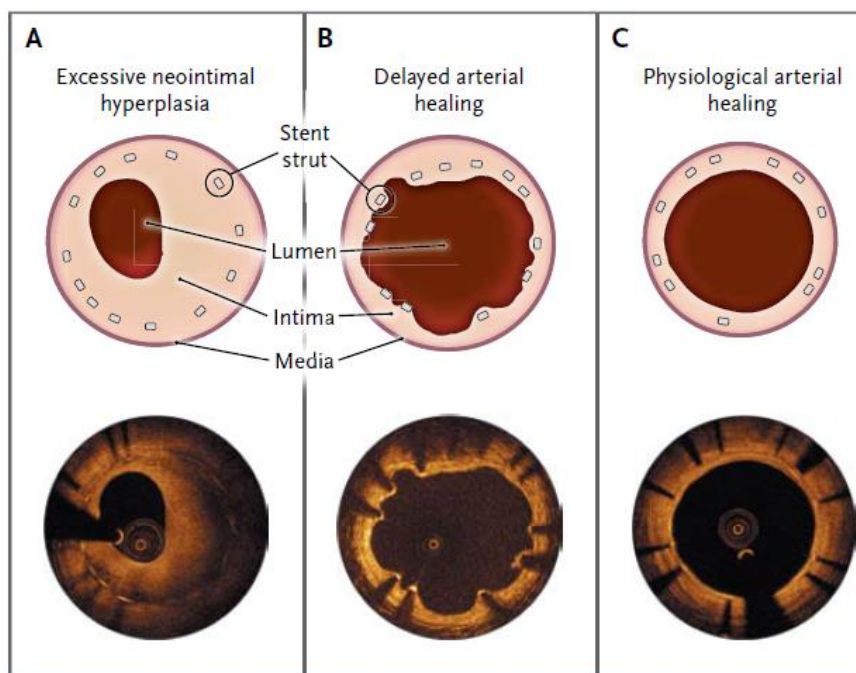


Figure 6: Representation with corresponding optical coherence tomography image of possible healing patterns in a stented artery by Stefanini and Holmes. (A) Excessive neointimal hyperplasia leading to restenosis, (B) delayed arterial healing with significant outpouching regions, or (C) physiological arterial healing are all possible healing patterns from a stent.

There are three types of stent malapposition: acute, late-persistent, and late-acquired stent malapposition (Im et al., 2014). Acute stent malapposition is a malapposed stent detected immediately after stent implantation, while late-persistent is a malapposed strut detected at follow-up that was present immediately after stent implantation and late-acquired is a malapposed strut detected at follow-up that was not present immediately after stent implantation (Im et al., 2014). Furthermore, late-acquired stent malapposition may constitute a potent substrate for late stent thrombosis after DES implantation (Im et al., 2014). Collectively, areas of uncovered struts, evaginations (outpouching regions) and large arcs of malapposition alter the blood flow patterns, affecting the reaction of the vessel wall.

1.4 Restenosis and Stent Geometry Causing Blood Flow Alterations

As described above, the coronary artery's reaction to a stent may progress in a variety of ways. The most common outcome is restenosis of the arteries. Furthermore, NT is the most common cause of restenosis, which alters the hemodynamics, or blood flow patterns, in the stented region (Chiastra et al., 2013). These altered blood flow patterns affect how smooth muscle or EC responds to the mechanical forces that are exerted on them. The mechanical forces of flowing blood may differ depending on the magnitude, directionality, and temporal fluctuations (Van Der Heiden et al., 2013). Research has shown that low time-averaged and/or oscillatory wall shear stress (WSS) promotes inflammatory activation and apoptosis of EC, whereas higher uniform WSS exerts protective effects (Van Der Heiden et al., 2013). The fact that the endothelium is differentially affected by high or low WSS and by unidirectional or bidirectional WSS seems to explain the focal nature of atherosclerosis, and also seems to play a role in arterial healing after stent deployment as a function of stent geometry (Van Der Heiden et al., 2013). For example, an alteration in the blood flow patterns in NT on the inner lining of the vessel wall has been investigated and has been shown to lead to persistent low time-averaged wall shear stress (TAWSS) (Chiastra et al., 2013).

The mechanical environment of the vessel wall is greatly affected by stent geometry and placement (Chiastra et al., 2013; Murphy & Boyle, 2010; Van Der Heiden et al., 2013). On the local scale, the design of the stent struts is especially relevant (Van Der Heiden et al., 2013). The presence of stent struts leads to perturbations in the local flow patterns, thus small regions of flow reversal and disturbed WSS will develop between the linkages of the stent (i.e. struts) (Van Der Heiden et al., 2013). Furthermore, stent strut malapposition, or tissue resorption between the stent struts, might reinforce local flow recirculation (Van Der Heiden et al., 2013). These local alterations in blood flow patterns may result in non-uniform forces on the vessel wall, which

signals a different intracellular signaling pathway than uniform flow as documented by Van der Heiden et al in Figure 7 below.

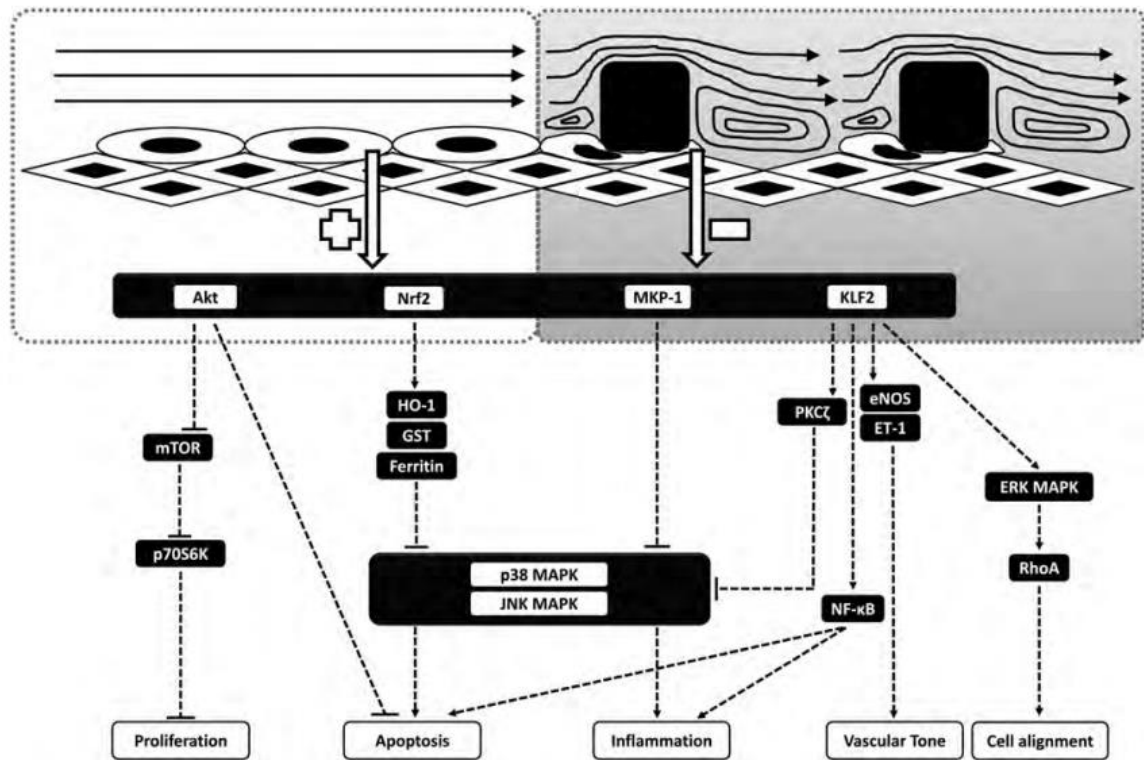


Figure 7: Contrasting signaling pathways for uniform flow (left) vs non-uniform flow (right) schematically described by Van der Heiden et al.

Stent geometry has been shown to locally influence WSS alterations and correlate with NT (LaDisa Jr. et al., 2005). Gundert et al employed blood flow simulations on idealized stented coronary arteries, which allowed for the creation of a hierarchy of stent design factors that can result in adverse WSS distributions (Gundert, Dholakia, McMahon, & LaDisa Jr., 2013). The authors found that strut thickness had the greatest impact on adverse WSS distributions. This metric of stent geometry was similar among stent designs. Stent-to-lumen area ratio, angle of struts relative to the primary direction of blood flow, and arrangement of connector elements were also predictive of adverse WSS distributions. This relationship, explored by Gundert et al, shows the impact a given stent geometry can have on the outcomes of specific coronary stents, which are also of importance for the current study.

1.5 Methods for Quantifying Intravascular Efficacy and Hemodynamic Impact of Stents

Imaging modalities, as well as image-based computational fluid dynamics (CFD), are vital and effective tools in determining the efficacy of stents. The improvement of imaging modalities, which thereby improves detail that can be included in CFD simulations of local changes in WSS indices, leads to a better understanding of the outcomes of stents. This ultimately leads to the future improvements of stents. Methods to determine the efficacy of coronary stents include intravascular ultrasound (IVUS), and optical coherence tomography (OCT), among others.

1.5.1 Intravascular Ultrasound

Intravascular imaging plays an important role in monitoring the progress of the stented artery as well as in the accurate placement of coronary stent in the target lesion. IVUS is an imaging modality that uses a catheter to acquire cross sectional images of an artery using ultrasonic sound waves to readily detect the presence of NT obstructing the stent, device under expansion, or edge problems (Alfonso, Byrne, Rivero, & Kastrati, 2014). IVUS is also a useful tool in detecting stent malapposition, as seen in previous studies (Im et al., 2014). IVUS, however, may not completely detect stent malapposition because of its limited axial resolution (100-200 μ m) or stent-related artifacts (Im et al., 2014).

1.5.2 Optical Coherence Tomography

OCT provides a much better axial resolution (12-18 μ m) than IVUS, yielding detailed images of the vessel lumen interface, the neointimal tissue, and the strut distribution (Alfonso et al., 2014; Im et al., 2014). These higher resolution axial images may detect stent malapposition with greater accuracy (Im et al., 2014). The optical light used to generate these higher resolution

images only has the fault of poorly visualizing residual plaque behind the stent as a result of lower tissue penetration compared with ultrasound (Alfonso et al., 2014). A comparison of OCT to IVUS modalities can be seen in Figure 8.

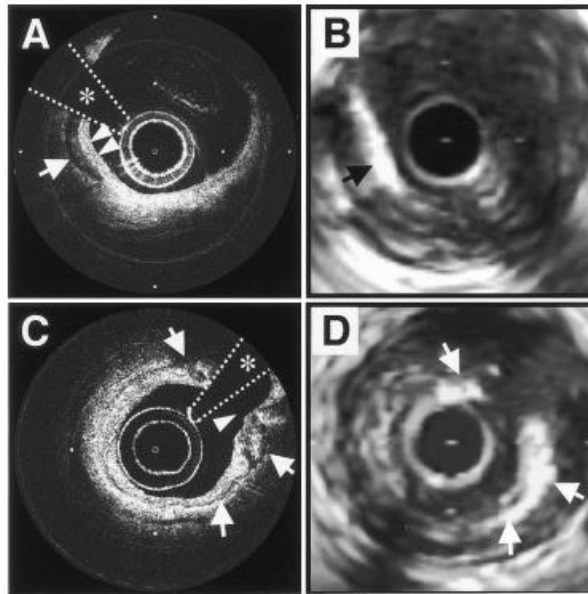


Figure 8: Comparison of intravascular imaging modalities (A and C = OCT, B and D = IVUS) of coronary plaques in vivo by Jang et al

1.5.3 Computational Fluid Dynamics

With the advancements in computational methods over the past two and a half decades, CFD has emerged as a powerful tool to assess the hemodynamic impact of coronary stents, whether positioned in idealized or patient-specific vessels (Arzani, Gambaruto, Chen, & Shadden, 2016a, 2016b; Chiastra et al., 2013; LaDisa Jr. et al., 2005; Morlacchi & Migliavacca, 2013; Morris et al., 2015; Murphy & Boyle, 2010; Vergallo et al., 2014). CFD offers the possibility to investigate local hemodynamic indices of stented coronary arteries at a level of detail not always accessible with experimental techniques (Chiastra et al., 2013) as discussed in more detail below. This computational approach combined with high resolution intravascular images allows for the accurate reconstruction of stented coronary arteries and the employment of patient-specific flow metrics to correctly quantify hemodynamic indices at the local and global level.

1.6 Hemodynamic Indices

Specific hemodynamic indices can be defined to characterize the hemodynamic forces exerted on the EC. Traditionally, WSS, which generally describes the tangential frictional force on the endothelial surface, is determined by the pulsatile flow in combination with the complex geometric structure of the vessels (Nordgaard et al., 2010). WSS (τ_w) is proportional to the wall shear rate ($\dot{\gamma}_w$) and the dynamic viscosity (μ) and can be expressed as:

$$\tau_w = \mu \dot{\gamma}_w \quad (1)$$

Another hemodynamic index that has been traditionally reported is the oscillatory shear index (OSI), which quantifies the change in direction and magnitude of the WSS and is calculated as follows:

$$\text{OSI} = \frac{1}{2} \left(1 - \frac{\left| \int_0^T \tau dt \right|}{\int_0^T |\tau| dt} \right) \quad (2)$$

where T is the period of a cardiac cycle and τ is the WSS vector (Nordgaard et al., 2010). This measure ranges from 0 to 0.5, where 0 describes a total unidirectional WSS and 0.5 represents purely oscillatory shear flow with net magnitude WSS (Nordgaard et al., 2010) equaling zero. Areas of high OSI have been reported to be predisposed to endothelial dysfunction and atherogenesis (Davies, 2009).

Recent advancements in the characterization of the near wall hemodynamic patterns has introduced new hemodynamic indices that shed light on the mechanical forces acting on the EC. Using the WSS trajectories to provide an approximation of the near-wall blood flow velocity, Arzani et al proposed a novel measure called WSS exposure time (WSSET) for quantification of

near-wall stagnation and concentration (Arzani et al., 2016b). The near wall fluid velocity can be represented based on the WSS vector field to first order as

$$u_{\pi} = \frac{\tau \delta n}{\mu} + O(\delta n^2) \quad (3)$$

where u_{π} is the velocity vector in the local wall tangent plane, τ is the WSS vector, μ is the dynamic viscosity, and the δn is the distance normal to the wall where the velocity is being evaluated (Arzani et al., 2016a, 2016b). The vector field defined by the first term of the right hand side of the Equation 3 represents the near wall fluid velocity and WSS trajectories are seeded on the entire region of interest uniformly and integrated based on near-wall fluid velocity (Equation 3) for a user-defined number of cardiac cycles per patient (Arzani et al., 2016a). The location of the WSS trajectory seed points are also user-defined and for the given study were applied only to the stent wall surfaces in the CFD models. Since CFD simulations were conducted over multiple cardiac cycles and assumed to be periodic, this enabled the velocity data to be reused for the purposes of WSS trajectory integration over many cardiac cycles (Arzani et al., 2016a). With this capability, the WSSET can then be computed which is a measure of the concentration and amount of time that wall-generated species spend near the wall (Arzani et al., 2016b). This measure of concentration residence time quantifies what is expected to be a driving mechanism for atherogenic or thrombogenic processes (Arzani et al., 2016b). WSSET, which is defined for each surface element (e) (triangle) of the computational model as the accumulated amount of time of all WSS trajectories (p) visiting that element, is calculated as follows:

$$WSSET(e) = \sqrt{\frac{A_m}{A_e} \sum_{p=1}^{N_t} \int_0^T H_e(p, t) dt},$$

$$H_e = \begin{cases} 1 & \text{if } \mathbf{x}_p(t) \in e, \\ 0 & \text{if } \mathbf{x}_p(t) \notin e, \end{cases} \quad (4)$$

where A_e is the area of the element, A_m is the average area of all the elements, $\mathbf{x}_p(t)$ is the position of the near-wall WSS trajectory, H_e is the indicator function for element e , N_t is the total number of WSS trajectories released and \mathbb{T} is the integration time ($\mathbb{T} = 10$ cardiac cycles). As mentioned above, WSS data was assumed to be periodic to enable trajectory integration for such a time scale (Arzani et al., 2016b).

Spatial wall shear stress gradient (WSSG) represents a commonly reported metric used in CFD studies that provide more information about the impact of WSS vectors on the surface of CFD models (Ladisa et al., 2005; Murphy & Boyle, 2010). Deformations in vessel geometry would alter the velocity vectors representing the movement of blood near the vessel wall, which would in turn affect WSS values on the vessel wall, and thereby would affect the WSSG metric. WSSG has been correlated with site susceptible to NT in an end-to-side anastomosis model and rabbit iliac model, where WSSG exceeded 200 N/m^3 (Murphy & Boyle, 2010). Areas of a vessel subjected to high WSSG represent areas of nonuniform WSS vectors. A stent geometry imposed on the vessel wall then would significantly influence the WSSG (Ladisa et al., 2005). LaDisa et al described how stent deployment creates polygonal cross sections of the vessel walls and as compared to circular cross section assumed in other CFD studies and how these different geometries affect WSSG (Ladisa et al., 2005). It was found that the polygonal cross sections, accurately reflecting vascular conformation, leads to increased areas of high WSSG, which may be associated with subsequent NT (Ladisa et al., 2005). The current study applies a modified representation of WSSG by calculating WSS variability in circumferential locations corresponding to OCT data, and quantifying changes in the segments axially along the length of the stented vessel.

1.7 Objective and Specific Aims

The overall objective of this research is to describe how WSS and other indices derived from WSS affect restenosis or resorption. More specifically, there is limited data on the correlation between WSS data and NT for current generation DES. In shedding light on this relationship, the potential clinical benefit of this research is that it may ultimately allow for a reduction in repeat revascularization procedures, in turn reducing the cost of healthcare and enhancing the wellbeing of patients receiving DES.

This project specifically evaluated three different DES consisting of different stent geometries as well as different drug-elution agents on their respective strut surfaces, and implanted into patient-specific coronary arteries. Hemodynamic indices were quantified immediately after stent implantation and their relationship to NT, or the opposite effect (vessel resorption), at 9-months follow-up were correlated. The three stents evaluated were the Nobori (Temuro), Promus Element (Boston Scientific), and Xience Prime (Abbott Vascular) DES. The objective was addressed through the specific aims described below.

Specific Aim 1: Evaluate the ability of traditional and recent WSS indices locally to predict neointimal thickening, or conversely, arterial resorption after drug-eluting stent implantation.

The first aim of this study was to locally analyze WSS indices and their predictive relationship to follow-up NT. In previous research, stent geometry has been shown to affect WSS distributions, which, in turn, affect NT (Gundert, Marsden, Yang, Marks, & LaDisa, 2012; Van Der Heiden et al., 2013). Specifically, previous research has shown that areas of low WSS and high OSI correlate with areas of the greatest NT growth following stent implantation (LaDisa Jr. et al., 2005; Murphy & Boyle, 2010; Van Der Heiden et al., 2013). The normal range of WSS magnitudes for an artery ranges from 10-70 dynes/cm² (Malek & Alper, 2014). Detailed stent

geometries, along with its variety in designs, can result in adverse WSS, or WSS magnitudes outside the range in a normal artery. This phenomenon was investigated by Gundert et al, who created a hierarchy of stent design factors that can result in adverse WSS (Gundert et al., 2013). Previous research also showed that areas of elevated spatial WSS gradients that occur with a specific stent geometry may be an important determinant to stent-induced changes in WSS and subsequent NT formation (Ladisa et al., 2005; Murphy & Boyle, 2010). There has been limited research regarding this relationship for first generation DES and they yielded conflicting results (Gijssen et al., 2003; Papafaklis et al., 2010; Suzuki et al., 2008). The outcome of this study builds on previous research by aiming to determine if local WSS analyses are enough to predictively identify locations of restenosis or resorption utilizing post-stenting WSS metrics.

Specific Aim 2: Use cluster analysis to uncover which stent design and/or patient-specific attributes correlate with neointimal thickening or vessel resorption using complex drug-eluting stent datasets containing traditional and recent WSS indices.

The second aim of this study was to collectively analyze WSS indices and their predictive relationship to follow-up NT, to determine the overall predictive hemodynamic metric and its relationship to NT. To achieve this aim, a collection of 29 different stented lesions were locally analyzed quantifying post-stenting WSS indices in the stented region amassing 469 slices. Two-step cluster analysis allowed for the collective understanding of the local relationship as compared to the individual relationships targeted in Aim 1. The collective local analysis of this aim shed light on current generation DES and the potential ability of a hemodynamic metric in its predictability of positive or negative remodeling.

Chapter 2

Methods

2.1 Preprocessing

2.1.1 Data Acquisition

Computed tomography angiography (CTA) and OCT imaging were performed immediately after stenting as well as at a nine-month follow-up. CTA is a noninvasive imaging technique that allows for accurate detection and exclusion of CAD in symptomatic patients (Bittencourt et al., 2014). There are some specific technical issues with CT imaging of the metallic coronary stent where the metallic struts cause an artifact known as the blooming effect (Mahnken, 2012). This effect causes the struts to appear thicker than they are, resulting in a misrepresentation of lumen volume in the stented region (Mahnken, 2012). Therefore, high resolution intravascular OCT imaging was used to accurately characterize the vessel geometry where the stent is present, avoiding the CT artifact in the stented region. The acquisition of this data was performed by Dr. Hiromasa Otake and his team at Kobe University Graduate School of Medicine in Kobe, Japan. This study was approved by the ethical committee of Kobe University and Institutional Review Board at Marquette University. CTA was performed using a 320-detector row CTA (Toshiba Aquilion One TM, Otawara, Japan) in accordance with guidelines set by the Society of Cardiovascular Computed Tomography (Abbara et al., 2009; Hughey, 2014). An intravenous bolus (30-90ml) of contrast agent was injected at a flow rate of 0.07ml/kg/s. The tube current type product was 300-400 mAs and a tube voltage of 100 or 120 kVp was used (Hughey, 2014). Scans were performed using ECG-based tube current modulation or sequential image acquisition (Hughey, 2014). Transaxial images were reconstructed with 0.75 millimeter slice thickness and 0.3 millimeter slice increment using a medium-smooth convolution kernel (Hughey, 2014). The acquisition of OCT images targeted the stented region, where stented OCT

images spaced 1mm apart axially were collected. OCT images for the regions distal and proximal to the stented region were provided for some, but not all cases. Therefore, CTA data was used to characterize the vessel distal and proximal to the stented region as well as any branching vessels in the stented coronary artery.

Coronary CTA data was visualized using VolView (Kitware, Clifton, NY). VolView is an open-source visualization tool capable of loading volumes designed for examination of medical data. For this specific project, VolView was used to visualize and create 3D volumes from CTA data within the stented coronary arteries.

ITK-snap (www.itksnap.org) was also used to visualize the CTA data and further target the stented artery to isolate the geometry of interest for model creation. ITK-snap is free open-source software that allows the user to interactively label structures in 3D medical image volumes. ITK-snap is also able to load a variety of file formats to visualize the data and further label the structures of interest. For this specific project, ITK-snap played an important role with its capability to isolate patient-specific blood vessel geometries in the vessel reconstruction steps. A patient-specific coronary tree model generated from ITK-snap is shown in Figure 9:

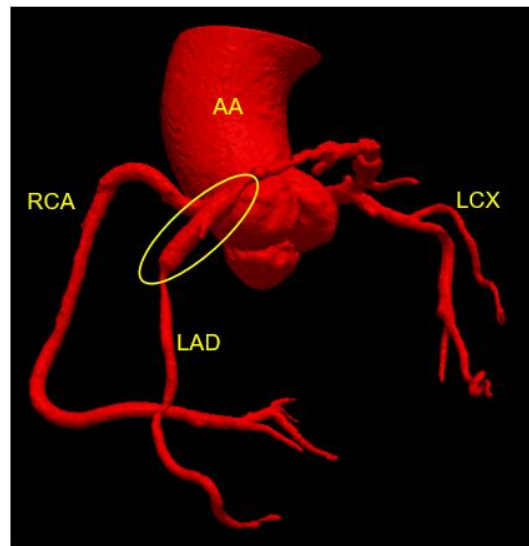


Figure 9: Surface model of the coronary tree. Ascending Aorta (AA) with Left Anterior Descending (LAD), Left Circumflex (LCX) and Right Coronary Artery (RCA) labeled. Stent placement in LAD is circled in yellow.

3D segmentation of the vessel using CTA was performed using a Hounsfield intensity lower only threshold of 175 HU and snake propagation of 25 iterations, as previously done by Antiga et al (Antiga & Steinman, 2014). The lower threshold coupled with the Hounsfield intensity was determined by comparing the segments generated from the CTA and the OCT data.

2.1.2 Patient-Specific Vessel Reconstruction

The patient-specific vessel reconstruction was divided into five distinct steps: (1) image processing, (2) wire pathway reconstruction, (3) segment registration, (4) model assembly, and (5) stent implantation. This process was created and validated by Ellwein et al (Ellwein et al., 2011). These steps are summarized below; additional details and developments to this procedure are highlighted here as well.

i. Image Processing

OCT images were processed using Matlab (MathWorks; Natick, MA). Lumen and stent contours, defined by the different color markings placed on the OCT images by the clinician, were first isolated and converted to grayscale. Unwanted text headers as well as other markings were masked from the image and then converted to a binary image. This final binary image is of the specified isolated contours only. An example of this is shown in Figure 10 below:

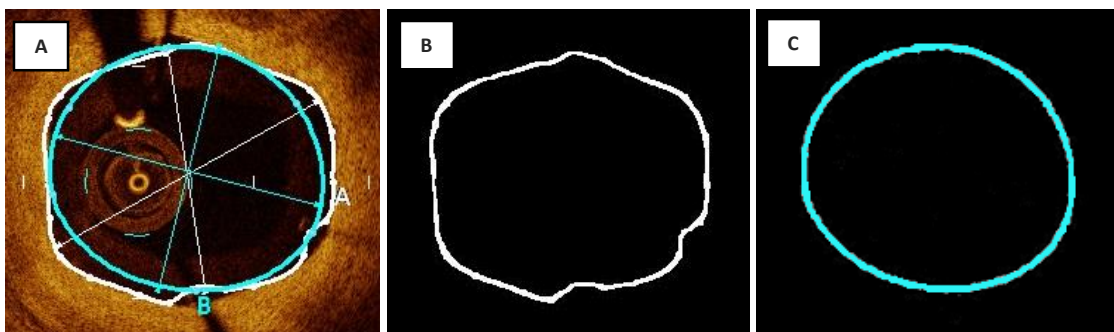


Figure 10: Binary image of lumen (B) and stent (C) contours from acquired OCT image (A).

OCT images were calibrated using ImageJ (www.imagej.net) by using a known distance scale provided on the images. This scale ensures that the cross-sectional shapes of the stent and lumen acquired from these OCT images are reconstructing accurately sized geometries.

ii. *Wire Pathway Reconstruction*

With OCT data acquisition, images were taken orthogonal to the optical lens which lies 24mm from the end of the 2.7 French Dragonfly catheter. Figure 11 shows a schematic of the OCT catheter.

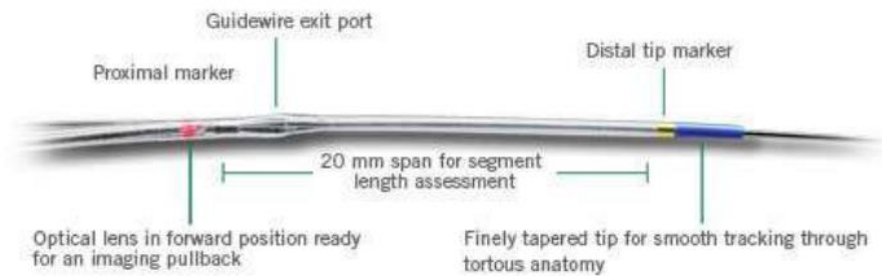


Figure 11: Schematic of OCT Dragonfly intravascular catheter (SJM, n.d.).

This catheter follows the guidewire path, which does not necessarily lie on the vessel centerline, indicating that the images may not necessarily be orthogonal images to the vessel being imaged. Therefore, the wire pathway needed to be defined for precise spatial reconstructed placement of the OCT images. The wire pathway was determined by using a minimum bending algorithm with a geometry of the artery as shown in Figure 12 and previously described in detail by Ellwein et al [34]. An example of the surface model generated from CTA and the corresponding wire pathway output reconstructed from the target vessel is shown in Figure 12 below.

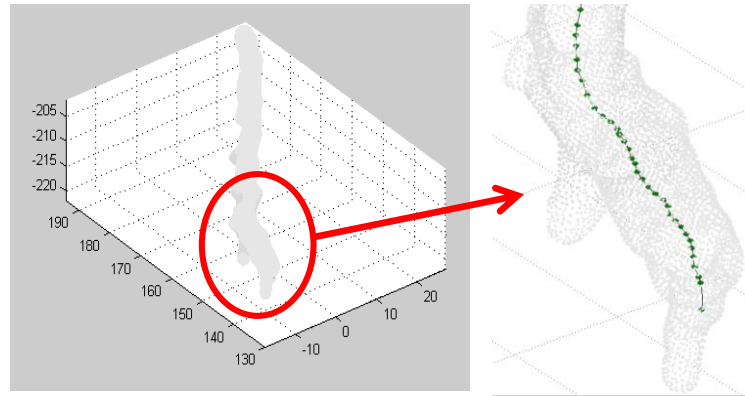


Figure 12: Wire pathway reconstruction Matlab output through stented coronary surface model

iii. Segment Registration

Segment contours from the OCT images were then registered on the reconstructed wire pathway using known landmarks from CTA such as the proximal end of the stent, distal ends of the stent or a bifurcation, where available. With the known OCT segment contours properly registered on the reconstructed wire pathway, the other OCT images were positioned longitudinally, according to OCT image spacing. For the given OCT image sets provided, the spacing between OCT images longitudinally was 1mm. Finally, OCT segment contours were oriented orthogonal to the wire pathway and rotated such that their centroids were aligned with the vessel centerline generated from the CTA data using open-source software ITK-Snap and VMTK (www.vmtk.org). The area of the generated segments from CTA and corresponding OCT images were compared using the 'group_calcAreas' built in function in SimVascular (<http://simtk.org/home/simvascular>). If the areas between CTA and OCT did not match, the threshold used for 3D segmentation was adjusted accordingly. This process was completed on a patient-to-patient basis. Both the segments generated from the CTA as well as the OCT in this segment registrations are shown in Figure 13, and were combined in the next step of the model creation process.

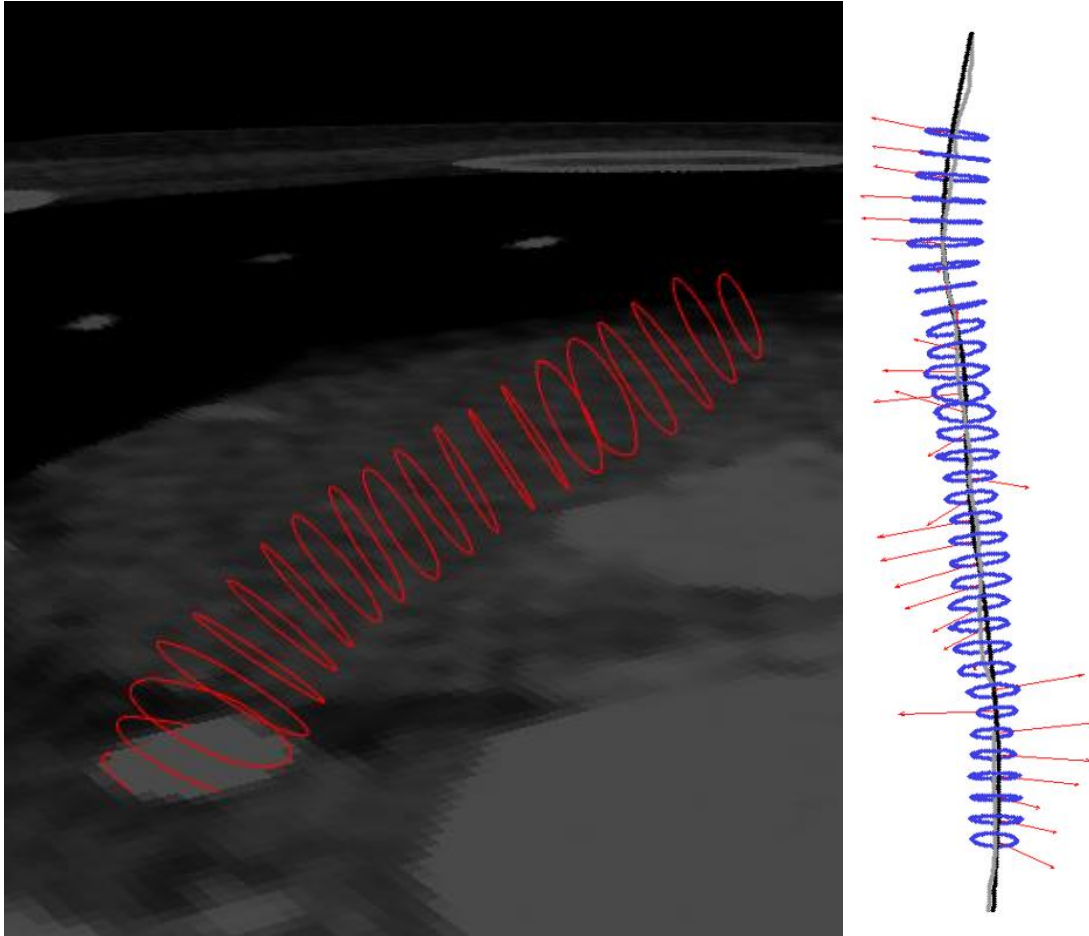


Figure 13: Segment creation from CTA data (left) and coregistered OCT segments (right) were used in conjunction to create patient-specific models. OCT segments were oriented normal to transducer path created through the wire pathway using an algorithm developed by Ellwein et al.

iv. Model Assembly

OCT segment contours from the stented region were coupled with CTA segment contours from the distal and proximal regions of the stent to create the entire vessel. The high resolution of the OCT segment contours within the stented region provides the detail needed to capture geometrical changes present in the lumen within the stented region, which is in the CTA segment contours due to the blooming artifact previously mentioned. Furthermore, OCT has been used in coronary arteries since 2007 in Japan and 2010 in the United States to analyze the efficacy of stent implantation offering 10 times the resolution of IVUS (Ellwein et al., 2011). The coupling

of OCT and CTA was critical for the accurate and complete assembly of the stented coronary artery model used in CFD analysis, which may uncover deleterious WSS indices and their potential relationship to NT after DES implantation. CTA segment contours were generated for branches within or near the stented region and were included since OCT images were not generated for these side branches. 3D representations of the proximal and distal regions to the stent were created using ITK-Snap and VMTK. Then customized Matlab scripts were used to create orthogonal segments defining the vessel lumen. The same Matlab scripts were used to create segments that represented the branch vessel lumen. Following this, the segments were imported into SimVascular. There the loaded segments were lofted for the vessel mainline, which included the stented, proximal and distal regions. Branches were also imported and lofted in SimVascular. Finally, the branches were added to the main vessel and blended to form a final Parasolid model (Siemens, Plano, TX) of the entire flow domain as shown in Figure 14 below.



Figure 14: Assembled lumen domain model from SimVascular.

In order to appropriately place the constructed models, conversions between the coordinate systems must be addressed. For example, SimVascular uses a coordinate system with an image origin at (0,0,0); however, ITK-Snap and VMTK use the NIFTI coordinate system. Equations to define these coordinate shifts were first implemented by Ellwein et al and were applied to convert between NIFTI and SimVascular coordinates, where (X_{sp}, Y_{sp}, Z_{sp}) were the spacings in the X, Y and Z directions, (X_o, Y_o, Z_o) were the coordinates of the Image Position (Patient) field (0020, 0032) of the most superior image, and N_{sl} was the number of slices in the data set. These shifts assumed that VolView placed the image origin at (-0.125, -0.125, -0.125) and images were 512 x 512. Employing these shifts properly resulted in segments that were registered with the stented vessel in SimVascular.

$$\begin{aligned}
X - Shift &= (-0.125 + 511 * X_{sp}) - (-X_0) \\
Y - Shift &= (-0.125 + 511 * Y_{sp}) - (-Y_0) \\
Z - Shift &= (-0.125 + (N_{sl} - 1) * Z_{sp}) - (-Z_0)
\end{aligned} \tag{5}$$

The process described above was also performed for the follow-up data. However, the follow-up lumen contours generated from the follow-up OCT images were used in the process. Furthermore, the post-stenting OCT images were co-registered with the follow-up OCT images. These image pairs were provided by Hiromasa Otake MD and his team to ensure the OCT images were paired appropriately and that the landmarks defining the OCT positions within the CTA data were appropriately placed.

2.1.3 Computational Stent Implantation

A series of Boolean operations were used to virtually implant each DES. These steps previously described in detail by Gundert et al (Gundert et al., 2011) are briefly reviewed here. First, a thick version of either the deployed Nobori, Promus, or Xience stent was created using SolidWorks (Solidworks Corp., Concord, MA). Stent platform geometries were acquired from the manufacturer and the specific stent cell pattern of each of the three stents analyzed in this study can be seen in Figure 15 below.

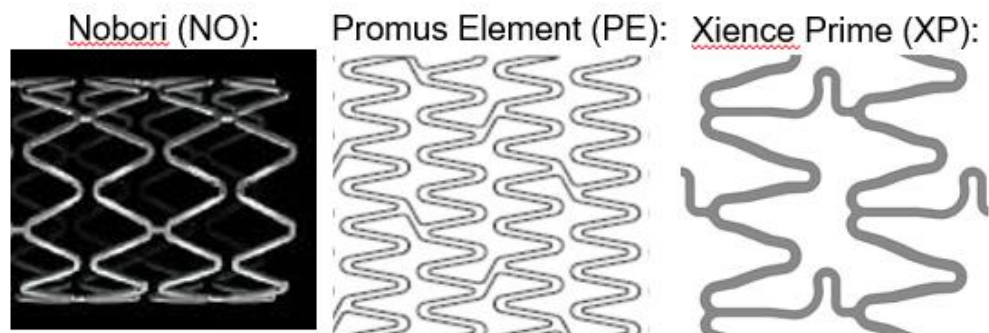


Figure 15: Nobori stent – Terumo (left, terumo_europe.com), Promus Element stent – Boston Scientific (middle, multivu.com), and Xience Prime Stent – Abbott Vascular (right, fda.gov).

The length of the stent was adjusted to match the length of the stent that was implanted in the patient. Further geometric details of each stent type can be seen in Table 1 below taken from Hughey et al (Hughey, 2014):

Table 1: Geometric specifications used in the creation of each stent type

	Nobori	Promus Element	Xience Prime
Strut Thickness (mm)	0.135	0.08	0.08
Strut Width (mm)	0.15	0.086	0.09

Next, a patient-specific stent domain Parasolid model was created from the marked stent contours on the OCT images. The patient-specific stent model was then converted to a shell model with the thickness of the shell matching the radial thickness of the manufactured stent used for that given patient. Following this, the thickened, length-appropriate stent was intersected with the patient-specific stent shell to give a patient-specific stent geometry. Finally, this stent geometry was subtracted from the lumen domain model to give a final blood flow domain model. These specific steps can be seen in Figure 16 below.

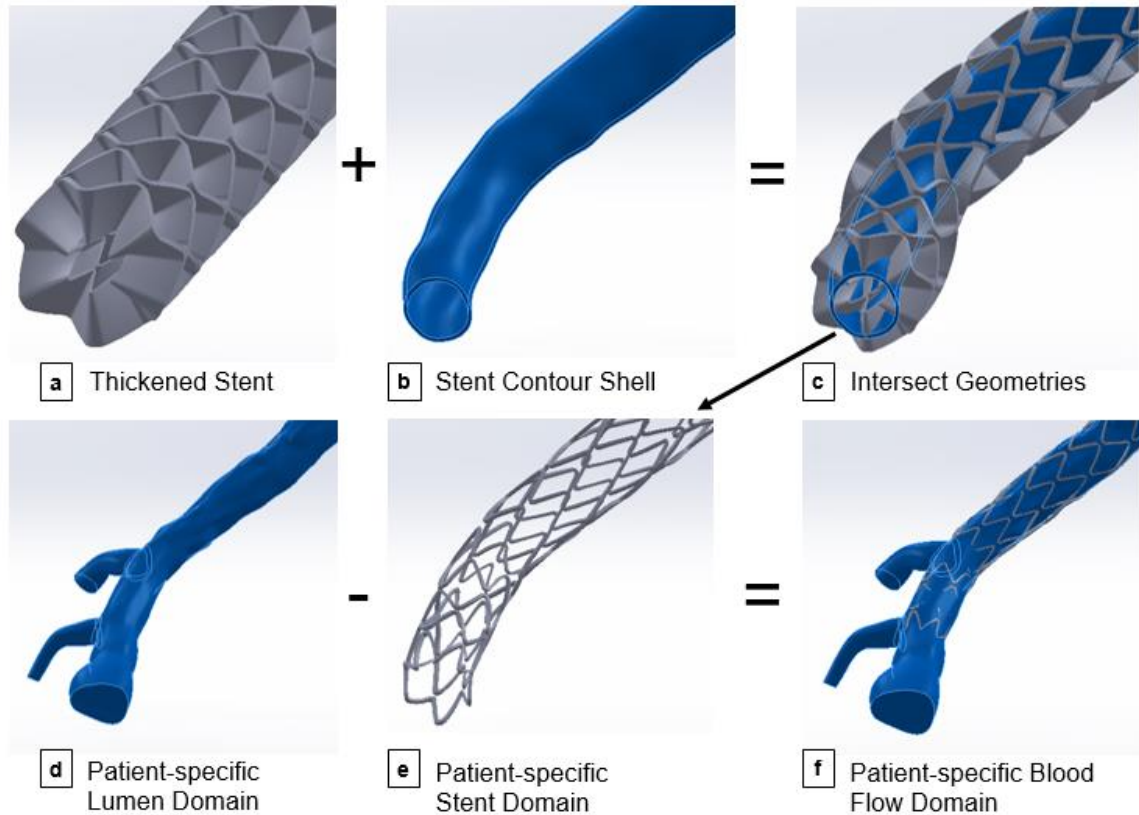


Figure 16: Boolean operation steps performed. Thickened stent (a) and stent contour shell (b) were intersected (c) to determine the patient-specific stent domain (e). Patient-specific stent domain was subtracted from patient-specific lumen domain (d) to obtain a patient-specific blood flow domain (f).

All the Boolean operations were performed using the “combine” feature in Solidworks. A final geometry analysis check was performed following these operations to ensure that discontinuous faces or discontinuous edges were not present in the blood flow domain model because CFD models need to be “watertight” to function (See Section 2.1.4 for the detailed stented model accuracy check). There are 2 types of discontinuities in geometric models: (1) discontinuity in the volume mesh, which would generate an artificial wall and (2) discontinuity in the surface of the model, which would produce an unrealistic outlet on the surface of the model.

It is worth noting that this methodology of computational stent implantation is not the only way stent geometries can be added to patient-specific vessel models. A structural finite

element analyses (FEA) approach to stent deployment in patient-specific geometries may be used to virtually implant a coronary stent (Chiastra et al., 2016). This FEA process requires a simulation to perform the virtual stent deployment, which, in theory, may allow for a highly accurate stented vessel model, since the process takes into account the local deformation of the artery lumen due to stent expansion (Chiastra et al., 2016). However, to accurately reproduce lumen dimensions and local geometric perturbations seen in associated OCT images, material properties for the healthy and diseased proportions of the coronary arteries would need to be obtained. However the healthy and disease portions of vessels are highly heterogeneous, and there is a paucity of data describing this heterogeneity. Moreover, the process of running a FEA simulation to obtain a geometry is computationally expensive (>24 hours on one node of a cluster) (Chiastra et al., 2016). Therefore, the Boolean operations performed for this study were substantially less computationally expensive, and likely more accurate, when compared to the FEA approach that would rely on the few published values for material properties in normal and diseased coronary arteries. The current approach instead employed a series of checks referencing stent positioning relative to OCT images to generate accurate patient-specific stented coronary artery models. Additional details are provided below.

The Boolean operations methodology mentioned above was originally done by Gundert et al using functions in SimVascular (Gundert et al., 2011). In the current study, these Boolean steps were performed in Solidworks, as previously mentioned. Earlier stented models also had the stent struts present without having the geometry being malapposed or free-floating stent struts (Hughey, 2014). The novel contribution of Hughey et al to this method was to include these malapposed stent struts (Hughey, 2014).

The current research improved this process by ensuring that the correct amount of malapposition, or lack thereof, was occurring in appropriate locations as dictated by OCT images from spatially equivalent regions. The centroid for the stent contour used the centroid of the

lumen contour. This made a substantial difference when the centroids were far apart as well as overall in that the models were being created with the highest amount of accuracy. Furthermore, to ensure that the calculation of follow-up NT was done accurately, rotation about the same centroid was necessary for corresponding follow-up images as well. An example of incorrect placement of the stent contour with respect to the lumen contour is shown in Figure 17 below.

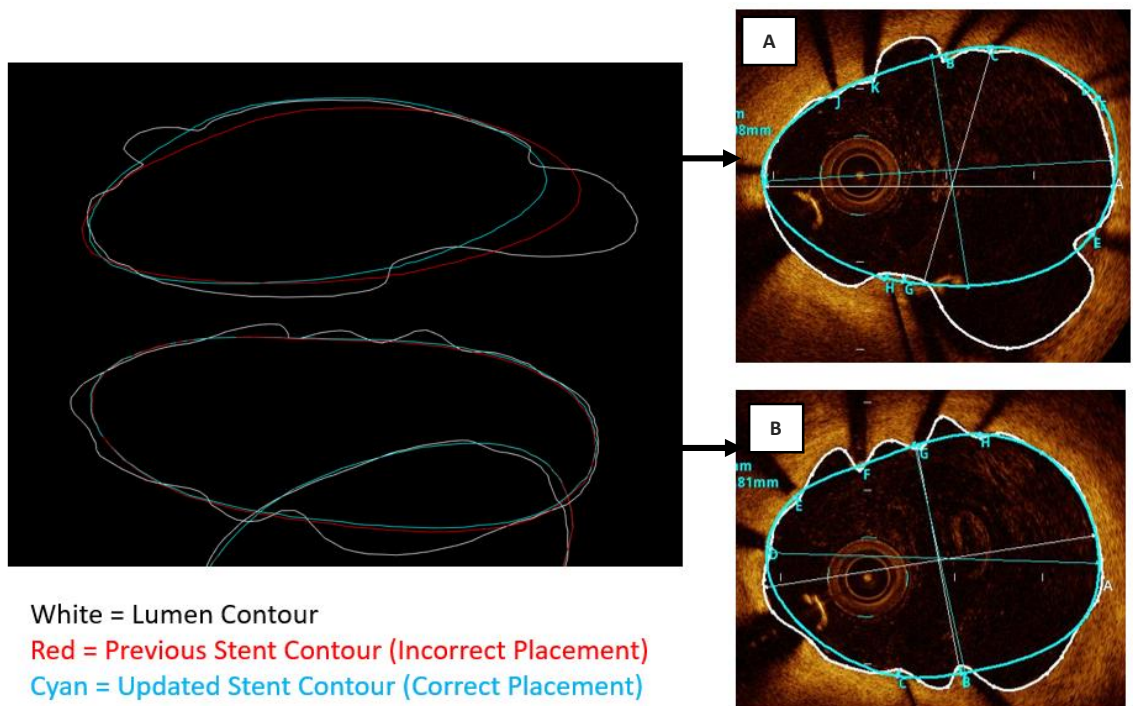


Figure 17: Methodology improvement showing accurate stent placement. Contours on left show previous placement (red) and updated placement. Corresponding OCT images on right show an example where improvement shows substantial change (A) and slightly noticeable change (B).

2.1.4 Stented Model Accuracy Checks

To ensure that the models were created accurately, several steps were taken as shown in Figure 18 below.

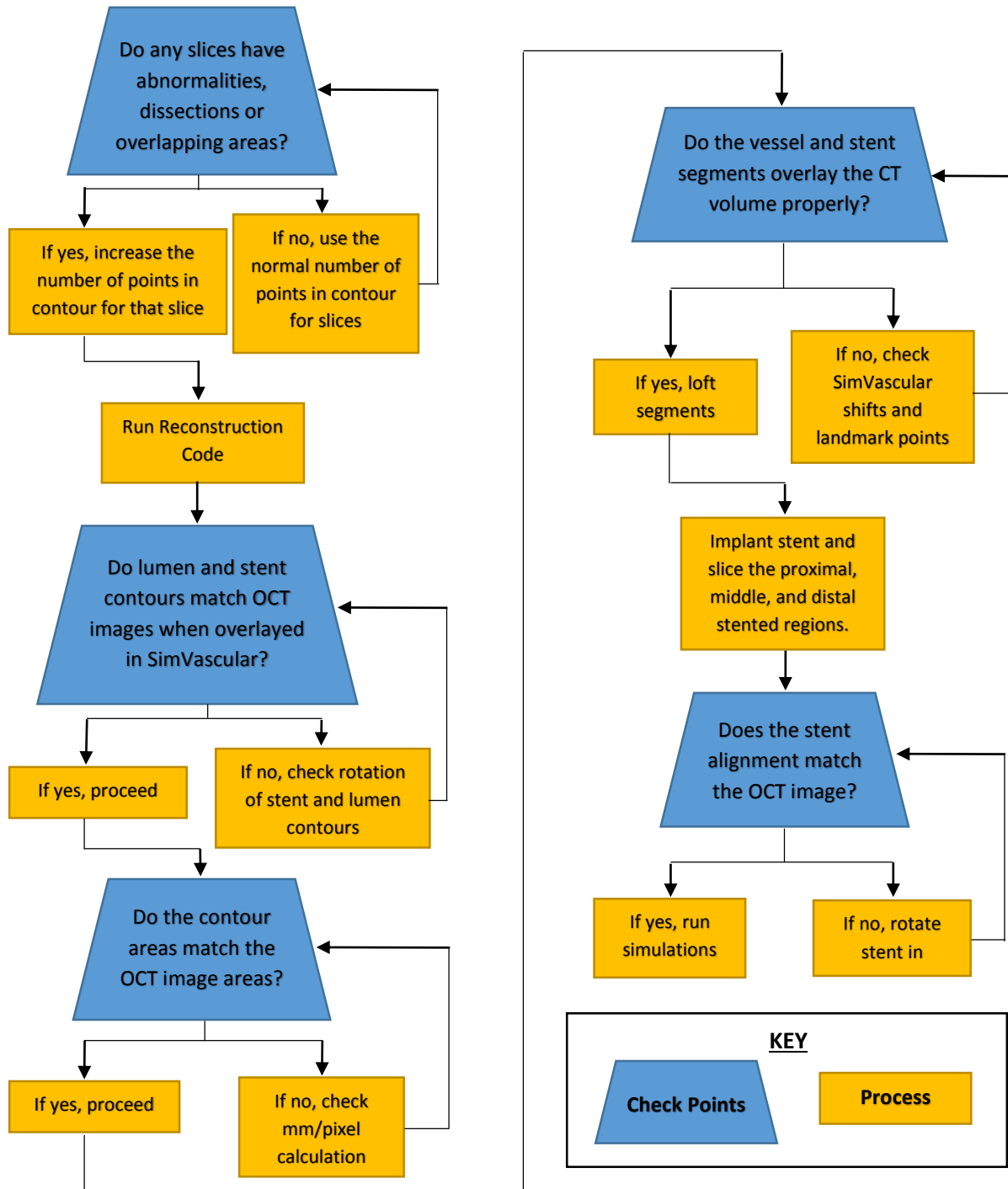


Figure 18: Check and balances of ensuring accuracy in model creation process (Hughey, 2014).

Previous generations of this research, conducted by Hughey et al, used SimVascular to perform Boolean operations, which did not specify model errors. Also, the methodology performed by Hughey required a mock simulation to obtain the .vtk file needed to observe stent placement within the model in Paraview. The current research methodology improved the previous process by using Solidworks and Paraview (Los Alamos National Laboratory, www.paraview.org) before loading the model into SimVascular to run the final simulation. By using Solidworks, the geometry of models can be observed directly in Paraview, which eliminates the need for a mock simulation. This new step expedited the stent placement process and allowed Boolean operation errors to be addressed effectively. The sequence of steps of this new method, following the Boolean operations in Solidworks, are (1) perform a Solidworks geometry analysis check, (2) export “watertight” geometry as an .stl file and load it into Paraview, (3) run Paraview script to observe stent placement and orientation, and (4) run custom Matlab script previously used by Hughey et al.

The new steps outlined above are given in detail as follows: First, a geometry analysis check is performed in Solidworks to determine if discontinuous geometrical entities are present in the stented model. If discontinuous entities were found in the model, they were corrected by rotating the thickened stent by less than 1 degree before the first Boolean intersect operation. If discontinuous entities persisted, then manual corrections in Solidworks were carried out to ensure a continuous blood flow domain model.

Second, the geometry is exported from Solidworks as an .stl file to be loaded into Paraview. In Paraview, the .stl file was found by opening all file types and then selecting “Stereo Lithography” from the list of available data readers. The transform feature was then used to scale the stent domain model by (0.001, 0.001, 0.001) for consistency in units between Solidworks and SimVascular. Finally, a .vtk file (ASCII format) was saved and used to check the circumferential positions of the stent struts within the vessel model.

The third step was to run the Paraview script to rapidly observe multiple stent placement and orientation. To observe the placement and orientation of the segments from the saved .vtk file, the precise OCT image locations represented by segments were used. Each segment contained the coordinates (origin and normal) of the OCT slices taken from the lumen OCT images used by SimVascular in the model creation process. This new addition to the current research allowed for the observation of all the OCT slices at once. A custom python script was developed to collectively slice the stent domain model. This script made observing and saving slices from a .vtk model efficient and allowed for rapid adjustment of the stent placement and orientation.

The fourth and final step was to run the orient.m Matlab script previously used by Hughey et al. The custom Matlab program compared the positions of struts in the stented model to the strut shadows produced in the analogous OCT images (Hughey, 2014). This script calculated a degree of rotation by taking three different OCT slices within the stented region (proximal, distal, and middle), based on the position of the struts, and calculated the average degree of rotation, and the stent was then rotated accordingly in Solidworks. The Boolean operations performed for virtual stent implantation were performed again, if needed, using the rotated version of the stent.

2.1.5 *Simulations*

i. Meshing

For each post-stent and follow-up model, an anisotropic mesh with unstructured tetrahedral elements was created using an automated mesh generation program (MeshSim, Simmetrix, Clifton Park, NY). A custom meshing macro allowed for different maximum element edge sizes on different model faces. This feature was used to place more elements in the flow domain where higher resolution of flow patterns are necessary to adequately capture irregular or

disorganized flow patterns occurring near the vessel wall and stent struts. Fewer elements were prescribed in the regions of the flow domain where a coarser density of elements was sufficient (i.e. intrastent regions and regions proximal and distal to the stent) to best resolve the near-wall hemodynamics without incurring the high-computational cost associated with dense isotropic meshes (Gundert et al., 2012; Hughey, 2014). An example of the generation of a discretized mesh from the generated Parasolid can be seen in Figure 19.

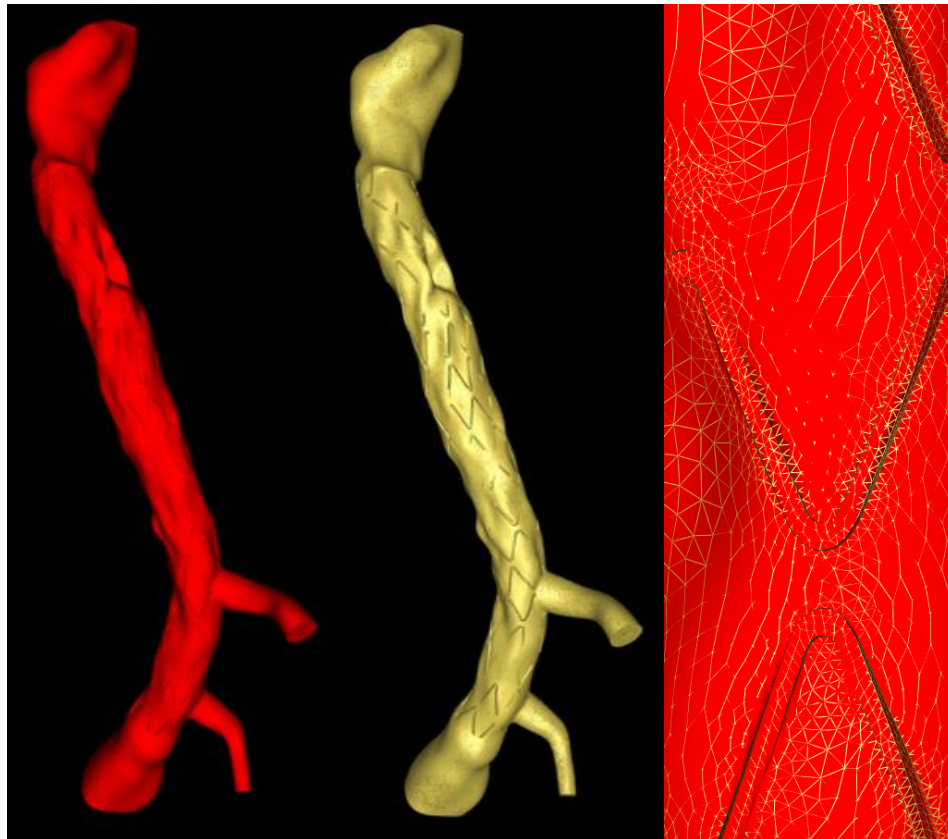


Figure 19: Patient-specific stented coronary model (left) and discretized model (middle). Close up of local mesh refinement (right) near stent struts increasing the spatial resolution in regions of potential adverse WSS

Mesh element sizes were based upon the strut width of the specific manufactured stent that was implanted. The maximum edge size at the stent face was set to $\frac{1}{4}$ the strut width (Hughey, 2014). Previous studies indicated that CFD results of the stented vessel model were independent of the mesh density using these mesh parameters (Gundert et al., 2012).

ii. *Boundary Conditions*

Post-stent and follow-up models were both subjected to a canine pulsatile blood flow waveform acquired from the left anterior descending coronary artery (Hughey, 2014; LaDisa Jr. et al., 2002). This blood flow waveform is associated with Reynolds and Womersley numbers defined for the left anterior descending artery, which made it applicable as in many previous computational studies (Ladisa et al., 2003, 2005; LaDisa et al., 2004; Williams, Koo, Gundert, Fitzgerald, & LaDisa, 2010). The mean blood flow through the stented artery was determined using cardiac output and assuming that the coronary arteries received 5% of the total cardiac output, of which the right and left coronary arteries received 16% and 84%, respectively (Ellwein et al., 2011; Hughey, 2014; Leaman, Brower, Meester, Serruys, & van den Brand, 1981). For patients whose cardiac outputs were not available, cardiac output and mean blood flow through the stented artery were determined using cardiac index and body surface area. A representative blood flow waveform was then scaled to match the mean blood flow of the specific vessel within the coronary tree and introduced at the model inflow face as a time-varying Womersley velocity profile (Hughey, 2014). For all simulations, blood was assumed to be a Newtonian fluid with a viscosity and constant density of 4cP and 1.06 g/cm³, respectively.

The flow split between the main vessel and subsequent branches was calculated assuming WSS autoregulation (i.e. Murray's Law). Murray's Law states that when a parent vessel branches into daughter vessels, the cube of the diameter of the parent vessel is equal to the sum of cubes of the diameters of the daughter vessels (Westerhof, 2010). For n daughter branches arising from a common parent branch:

$$r_p^3 = r_{d_1}^3 + r_{d_2}^3 + r_{d_3}^3 + \dots + r_{d_n}^3 \quad (6)$$

where r_p is the radius of the parent branch, and r_{d_1} , r_{d_2} , r_{d_3} , and r_{d_n} are the radii of the respective daughter branches. Murray's Law, or the principal of minimum work, represents an ideal

branching pattern that optimizes energy expenditure vs metabolic need, and appears to be mediated by variations in artery caliber induced by WSS (Hughey, 2014).

A three-element Windkessel model was implemented at each outlet of the models to replicate the physiological effect of the arterial tree distal to the vessel being analyzed. The three-element Windkessel model is comprised of three main parameters R_c , C and R_d (Hughey, 2014; Westerhof, 2010). R_c is the characteristic impedance representing the resistance, compliance and inertiance of the proximal artery of interest, C is the arterial capacitance and accounts for the sum of the compliance of the arteries beyond the model outlets, and R_d describes the distal resistance in the absence of ventricular contraction (Ellwein et al., 2011; Westerhof, 2010). For any given input flow, the total resistance (sum of R_c and R_d) can be adjusted to vertically shift the calculated pressure waveform, and the ratio of R_c/R_d as well as the C can be adjusted to modulate the shape and pulse amplitude of the calculated pressure waveform (Hughey, 2014; Kung, 2010). Once the appropriate component values for the three-element Windkessel have been determined to give desired pressure and flow for each outlet, then the target values in the design and construction of the outlet boundary conditions were considered (Hughey, 2014).

In the absence of ventricular contraction using the impulse response method demonstrated by Van Huis et al, R_c and R_d sum to be the zero hertz impedance (Z_0). Z_0 is between 22% and 65% less than the total resistance value (Van Huis, Sipkema, & Westerhof, 1987). Therefore, the mean blood pressure and mean flow for each patient was scaled by 65% for the data to be constrained within the range presented by Van Huis et al. With Z_0 obtained, it was necessary to determine R_c or R_d to characterize the Windkessel boundary condition described above. Therefore the characteristic impedance. Therefore the characteristic impedance (R_c) reflective of average impedance of frequencies above 7 Hz was used:

$$R_c = \frac{C_{ph}\rho}{\pi r^2} \quad (7)$$

where C_{ph} is the wave speed, ρ is the blood density, and r is the vessel radius.

A wave speed of 6.7 or 8.6 m/s was applied to represent either a left circumflex or left anterior descending canine coronary artery, respectively (Gow & Hadfield, 1979; Hughey, 2014; Williams et al., 2010). R_c was calculated for each outlet branch and R_d was calculated as the difference between Z_o and R_c . Capacitance at each outlet was calculated using a Matlab program implementing the Pulse Pressure Method of Stergiopolis et al, which determines pulse blood pressure based on an inflow waveform, the calculated R_c and R_d values (Hughey, 2014). Specifically, in the frequency domain, the Fourier transform of the flow waveform was multiplied by the impedance, which is calculated as shown in Equation 8 (Hughey, 2014).

$$Z(\omega) = R_p + \frac{R_d}{1 + j\omega CR_d} \quad (8)$$

The maximum (systolic), minimum (diastolic), and difference between the maximum and minimum (pulse pressure) was compared to the desired blood pressure values (Hughey, 2014) iteratively using this program, and the capacitance value was adjusted realizing that lower compliance yields larger pulse pressures and vice versa (Stergiopulos, Segers, & Westerhof, 1999). This method is further illustrated by Figure 20.

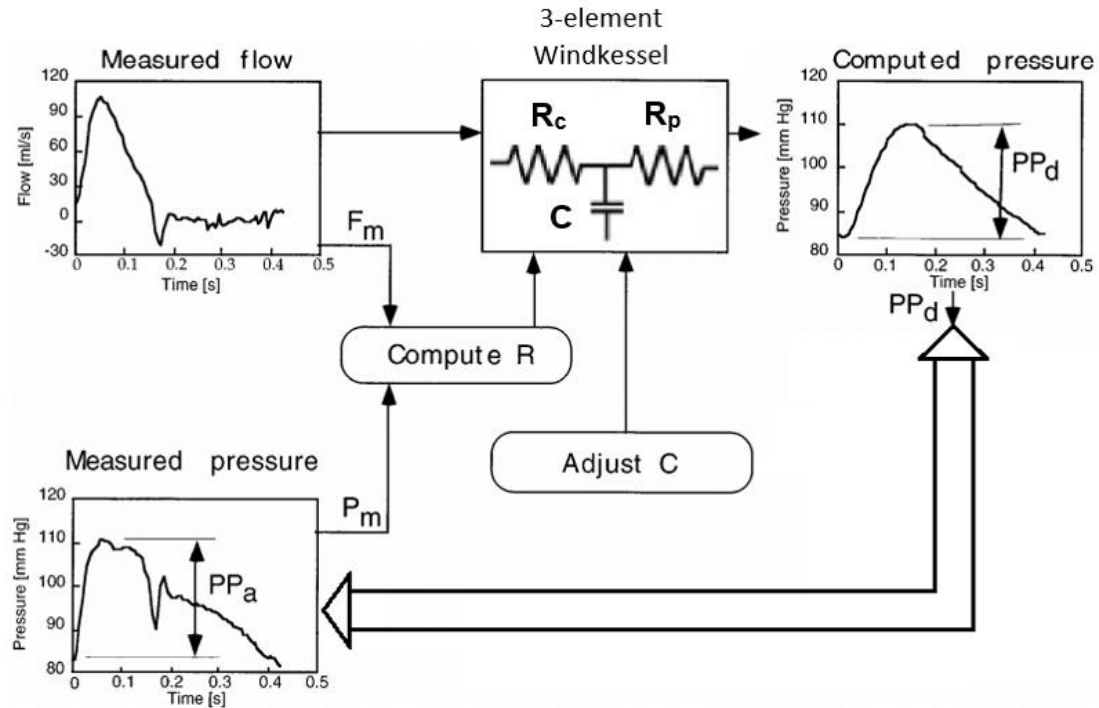


Figure 20: Using flow waveform, blood pressure, impedance spectra, and RCR parameters to replicate physiologic behavior (F_m =mean flow, P_m =mean pressure, R_c =characteristic impedance, R_d =distal resistance, C =capacitance, PP_d =pulse pressure predicted by model, PP_a =pulse pressure method) (Hughey, 2014). Image obtained from Westerhof, American Phys. Society, 1999.

iii. Governing Equations

Simulations were performed using a stabilized finite element method to solve equations for the conservation of mass (continuity) shown in Equation 9 and Equation 10 and balance of fluid momentum (Navier-Stokes) shown in Equation 11. The conservation of mass is defined using the continuity equation:

$$\frac{\partial \rho}{\partial t} + \nabla \cdot (\rho \vec{u}) = 0 \quad (9)$$

where ρ is density and \vec{u} is flow velocity. Since blood is assumed to have a constant density of 1.06 g/cm^3 , the divergence term factors out and the partial derivative is eliminated, thus simplifying to the continuity equation for incompressible flow:

$$\nabla \cdot \vec{u} = 0 \quad (10)$$

The conservation of momentum is defined using the Navier-Stokes equation:

$$\rho \left(\frac{\partial \vec{u}}{\partial t} + \vec{u} \cdot \nabla \vec{u} \right) = -\nabla p + \mu \nabla^2 \vec{u} \quad (11)$$

where $\frac{\partial \vec{u}}{\partial t}$ is temporal acceleration, $\vec{u} \cdot \nabla \vec{u}$ is convective acceleration, ∇p is the pressure gradient

and $\mu \nabla^2 \vec{u}$ is the diffusion of momentum.

Four cardiac cycles were performed for each simulation to ensure convergence with a maximum difference in blood pressure and flow between equivalent time points in successive cardiac cycles of less than 1 mmHg and 1mm³/sec, respectively.

2.1.6 Post-Processing

i. Data Normalization

WSS results obtained from the simulations performed were represented as the TAWSS values, which represent an average of WSS values calculated over the last cardiac cycle of the simulation as shown in Equation 12 below:

$$TAWSS = \frac{1}{T} \int_0^T |\vec{\tau}| dt \quad (12)$$

where T is the duration of the cardiac cycle. To increase confidence in aggregate results when comparing stented coronary models from different locations in the coronary tree and across patients, TAWSS results were normalized using TAWSS from the unstented region proximal to the stent. This normalization procedure, which should yield normalized TAWSS results ranging from 0 to 1 for each case, was previously performed by Hughey et al (Hughey, 2014). Also, the normalization process of TAWSS values produce a dimensionless quantity and are presented as

unit less values. As mentioned above, in performing this normalization step, one can compare the TAWSS results calculated from the simulations regardless of the location in the coronary tree, which ultimately accounts for the different inflow boundary conditions prescribed for each model. This normalization step is also desirable as the prescribed inflow boundary conditions are based on a variety of assumptions, and this normalization process mitigates any uncertainty arising in the collective results from those assumptions.

ii. Local Analyses

Normalized TAWSS results were quantified locally at slices corresponding to the specified OCT image sites that were used in the model construction process described above. Previously Hughey et al looked at 3 slices for a particular case (Hughey, 2014). In contrast, results in the current report for all WSS indices were obtained at slices corresponding to each specific OCT image location so that direct correlations could be made between the initial post-implantation stimuli and follow-up tissue growth. The number of slices analyzed in each case varied due to the length of the stent implanted for each case. A python script was created to quickly perform local quantification by reading the specific OCT slice orientation used in the model construction process. Figure 21 shows an example of the collective local analysis being performed on a given case.

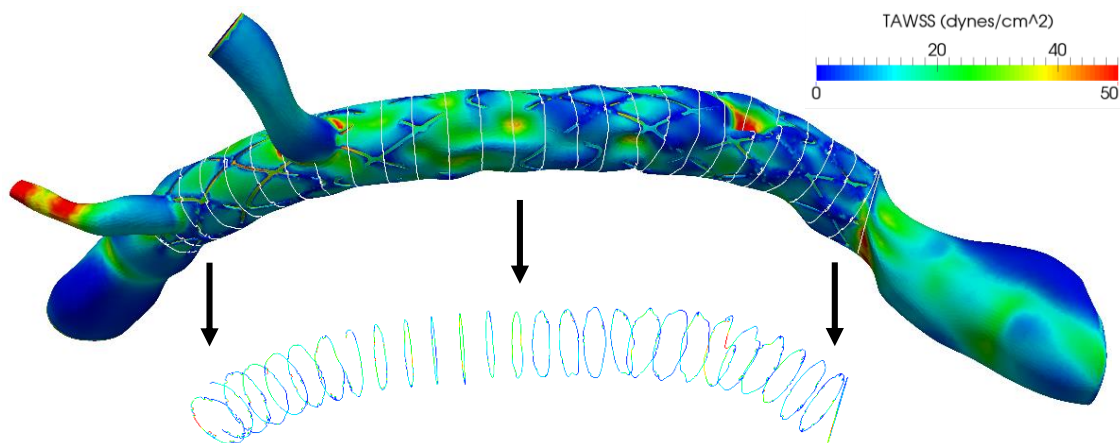


Figure 21: Local analysis of a case showing TAWSS. All locally analyzed slices reside in the stented region and correspond to OCT slices obtained.

iii. Isolation of Vessel Wall Indices

Previous local TAWSS quantification included both the lumen and stent TAWSS values, as shown in Figure 22a. However, including stent TAWSS values in the local quantification can induce high values of TAWSS measured on the stent faces due to the sharp edges prominent in the stent geometry if portions of the stent are not in direct contact with the vessel wall. Additionally, to characterize the reactionary behavior of the vessel at follow-up, stent TAWSS indices should not be included in the local TAWSS quantification as the cells on the inter luminal surface react to the TAWSS but are typically not present on the stent surface directly after stent implantation.

With the above in mind, an in-house algorithm was created to target only the data on the vessel wall. Each locally quantified TAWSS slice was divided into bins specified by the user. In each bin, the maximum distance from the centroid to any of the data points within that bin was identified and extracted through the algorithm. The extracted data points correspond with TAWSS on the vessel wall, excluding data points on the stent struts, as shown in Figure 22c. The steps of this algorithm can be seen in the Figure 22.

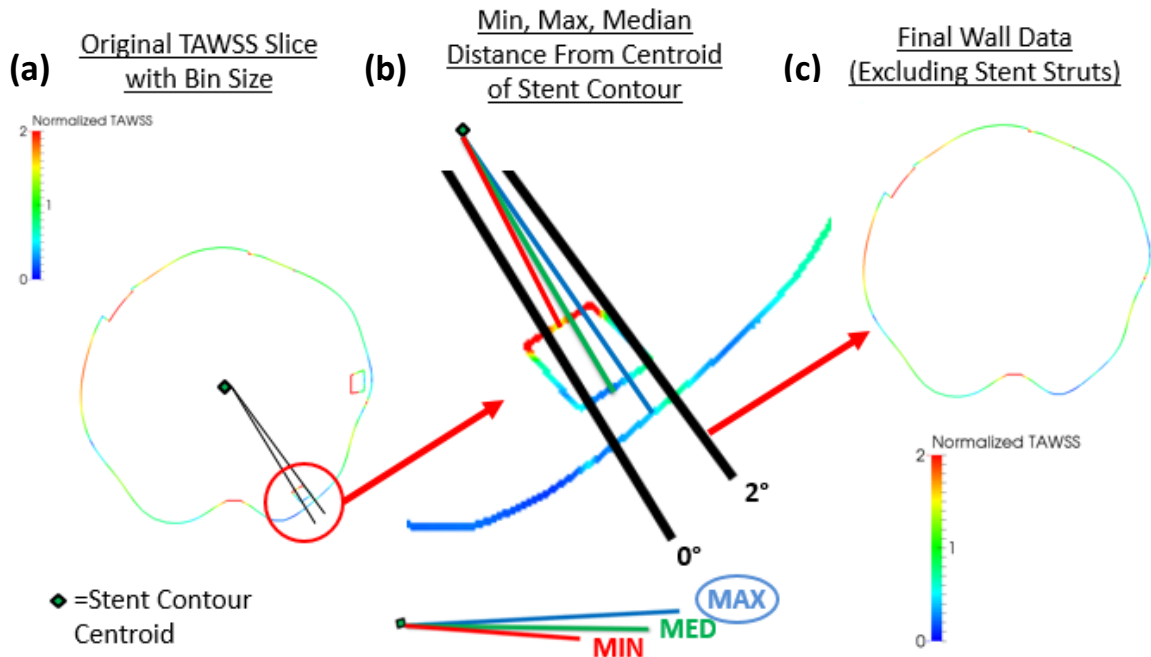


Figure 22: In-house algorithm developed to target only the data on the vessel wall, or in other words, excluding the values on the stent surfaces. Used bin setting (middle) to determine maximum distance from the centroid of that slice and keeps those values (right).

Only values on the vessel wall were included in the TAWSS and its derivative calculations. In other words, if a branch was present in the localized TAWSS results, then measured values of TAWSS present in the branch itself were not included in the analysis.

iv. Normalized TAWSS Variability

To further characterize the TAWSS patterns on the vessel wall, the normalized TAWSS variability was calculated in two steps: (1) the standard deviation of TAWSS was calculated for each slice; and (2) the central difference approximation to the second derivative (CDASD) of all consecutive slices within the stented region was calculated to relate the analyzed slice with its distal and proximal local analyses. The calculation of the standard deviation of TAWSS within each slice for step 1 was used because it is known to be a variability measure sensitive to outliers. Alternative measures of variability, such as the sum of absolute deviations, are less sensitive to outliers. The use of standard deviation was justified due to (1) the detailed nature of the three

different stent geometries used in this study and (2) the high resolution of OCT images used to define the geometry within the stented region of the CFD models.

Step 2 characterized how the TAWSS patterns changed along the length of the vessel. Equation 13 is the CDASD used to describe the variability of TAWSS from each local analysis to the next (Greenbaum & Chartier, 2012).

$$f''(x) \approx \frac{f(x+h) - 2f(x) + f(x-h)}{h^2} \quad (13)$$

where $f(x+h)$ is the TAWSS of the proximal slice, $f(x)$ is the TAWSS of the slice for which the second derivative is being quantified for, $f(x-h)$ is the TAWSS of the distal slice, and h is 1mm corresponding with the distance between TAWSS slices. Finally, the absolute value of the CDASD was calculated for each slice to indicate the overall magnitude of change in standard deviation along the length of the vessel. It should be stated that due to the 1mm spacing used for h , this approximation for the second derivative is a course approximation of the second derivative and should not be used as a replacement for the true second derivative calculation. Similar to TAWSS, TAWSS variability came from normalized TAWSS values, which produce a dimensionless quantity and are presented as unit less values. Figure 23 shows the way the TAWSS variability is calculated.

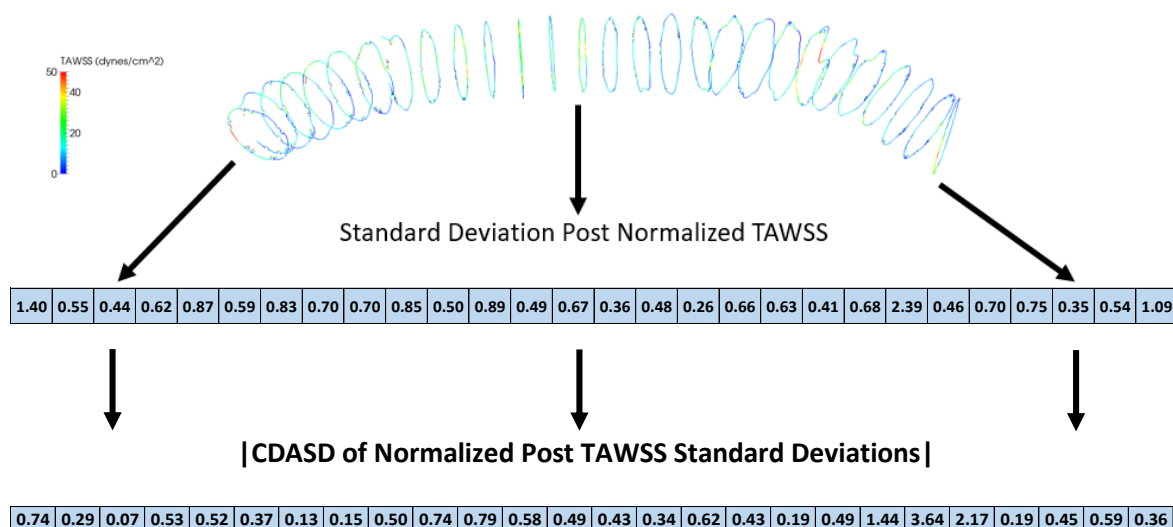


Figure 23: Quantification of TAWSS variability. Starting from the collection of local analyses (top), the standard deviation of TAWSS for each independent slice is calculated (middle). Then the absolute value of the CDASD is used to calculate the relationship between neighboring slices to determine the changing variability along the length of the stented region (bottom).

The motive of this approach was to characterize how normalized TAWSS was varying within a given OCT slice as well as how that variation related to the proximal and distal neighbors. This roughly represents a reduced-order, or less computationally-expensive, version of spatial WSSG metric mentioned in the introduction. The use of the second derivative initially came from previous research conducted by Ma et al (Ma, Harbaugh, & Raghavan, 2004). In this research, Ma et al developed second-order curvature-based indices to geometrically characterize cerebral aneurysms (Ma et al., 2004). Ma et al's research targeted the predictability of aneurysm rupture risk based on the unveiling of second-order indices (Ma et al., 2004). For the current study, the CDASD is applied to characterize how TAWSS variation may be occurring due to geometrical variabilities from the vessel and stent geometries.

TAWSS variability changes along the length of a stented vessel due to four main reasons. The first reason is stent geometry, where the stent geometry may be symmetric and periodic as with the Nobori stent type (peak-to-peak stent type) or the stent geometry may be asymmetric as with the Promus Element stent type (peak-to-valley stent type) and Xience Prime stent type

(peak-to-valley with extendable connectors stent type). The second reason is the patient vessel geometry, where bends, undulations and bifurcations in the vascular geometry changes the TAWSS variability metric. The third reason is how the stent geometry relates to the vessel geometry and vice versa, where the orientation of the stent in the vessel and the apposition of the stent to the vessel wall. The final reason is the fact that an idealized vessel with a narrowing does not change longitudinal TAWSS variability from slice to slice indicating the approach to characterize the TAWSS variability metric underscores the circumferential variability due to the first 3 reasons described above.

v. *Wall Shear Stress Exposure Time*

WSSET was determined from the vectorized form of WSS for each case and was defined for each surface element as the “accumulated amount of time all the trajectories visiting that element” over the cardiac cycle (Arzani et al., 2016a). Specifically, these are wall-generated WSS trajectories are prescribed by the user for a given surface on the CFD model and, for this research, were prescribed for the stent wall faces only. This was done to characterize the drug-elution behavior associated with DES and its potential relationship to NT or resorption. Previously, this metric was applied to characterize near wall stagnant flow in abdominal aortic aneurysms and is now being applied in stented coronary arteries to provide a better understanding of the regions of stagnant flow within the stented region (Arzani et al., 2016a). The measure of stagnant flow may be more useful in characterizing DES specifically since the elution agent, which inhibits neointimal remodeling, may reside in locations of high WSSET and therefore have an impact on vessel resorption. The WSSET index was also normalized prior to analysis, by way of dividing the WSSET results by the product of the period of the cardiac cycle for the given patient and number of cycles ($n = 10$ cardiac cycles) used to compute the WSSET results. This normalization step produced a dimensionless quantity which is reported as unitless and allowed for the

comparison of this metric for patients who have different cardiac cycle lengths. Furthermore, the isolation of only the wall values was performed using the same in house binning algorithm previously described.

vi. Local Change in Lumen Area between Post and Follow-Up OCT Pairs

Pairings of post-stenting and 9-month follow-up OCT images were provided by the collaborator who acquired the images and identified consistent positions along the length of the stented region. An example of these image pairings as provided by the collaborating clinician are shown in Table 2.

Table 2: Example of post-stenting to follow-up OCT image pairing provided by collaborators

	OCT image at post PCI	OCT image at follow-up
1	250	180
2	260	190
3	270	200
4	280	210
5	290	220
6	300	230
7	310	240
8	320	250
9	330	260
1 0	340	270
1 1	350	280
1 2	360	290
1 3	370	300
1 4	380	310
1 5	390	320

OCT image number 250 at post and 180 at follow-up are same cross section.

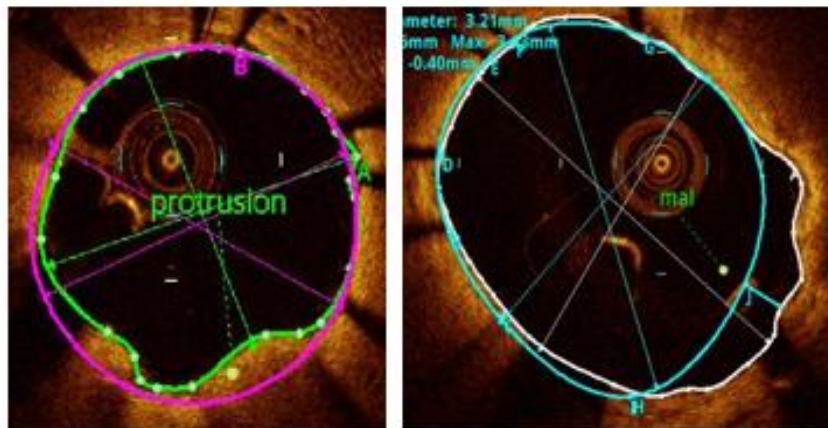
.

.

.

OCT image number 390 at post and 320 at follow-up are same cross section.

The percent change in lumen area (CLA) is calculated from the image pairs defined between post and follow-up OCT images. This index from post to follow-up gives a measured value of how the vessel has remodeling at the analyzed local OCT slice pair. An example of this local calculation of the CLA is shown in Figure 24.



Post
Lumen = 5.95mm²
Area

Follow Up
Lumen = 8.83mm²
Area

$$\begin{aligned} \text{Change in Lumen Area (CLA)} &= (8.83\text{mm}^2 - 5.95\text{mm}^2) / 5.95\text{mm}^2 * 100 \\ &= 48.4\% \end{aligned}$$

Figure 24: Calculation of CLA metric. Post-stenting (left) to 9-month follow-up (right) OCTs have lumen area calculations marked on the image which are used to describe the lumen area changing for each given OCT pair

A positive CLA indicates that the lumen area was larger at follow-up, which may be an indication of vessel resorption, and a negative CLA indicates that the lumen area was getting smaller at follow-up, which may be an indication of vessel restenosis.

vii. Average of Post-Stenting Metrics

Due to the analysis of the CLA that resulted in a single value, the post-stenting metrics calculated from the post-stenting model were averaged for each post OCT slice. The average of the post normalized TAWSS and average post normalized WSSET provided single values that summarized each metric for the post OCT slice, which was related back to the CLA at 9-months follow-up. The TAWSS variability metric, defined earlier, also provided a single value that was compared to its corresponding CLA. Prior studies have often simplified CFD results, by taking an average of values on a specific region on the computational model, to help interpret results more succinctly (Peiffer, Sherwin, & Weinberg, 2013). Data-processing methods that have been employed include axial averaging, circumferential averaging (performed in the current research), thresholding, visual comparison of maps, selective analysis, and descriptive analysis (Peiffer et al., 2013). Hughey et al performed thresholding on post-stenting models and summarized the differences in post-stenting metrics for the three different stent type coronary models investigated in this research (Hughey, 2014). The local description of CLA and the correlation back to a circumferential average for several indices was an approach to simplify, yet still capture, changes in the 9 months following DES implantation.

viii. Cluster Analysis and Supplemental Marker Indices

Two-step cluster analysis was performed using SPSS statistical software. The detailed approach of this statistical algorithm was first implemented by Chiu et al in 2001. In general, this multivariate, model-based technique can reveal the patterns of a large data set that may be masked or difficult to track when looking at each case individually. This two-step cluster approach allows for the inclusion of both categorical variables and continuous numerical variables when determining relevant patterns in the data. The relevant patterns in the data are based on a distance measure derived from a probabilistic model in which the distance between

two clusters is equivalent to the decrease in log-likelihood function as a result of merging (Chiu, Fang, Chen, Wang, & Jeris, 2001). The ability to include continuous as well as categorical variables was the motivation in using this two-step approach.

Cluster analysis is a convenient method for classifying homogeneous groups of objects called clusters (Sarstedt & Mooi, 2014). The objective of cluster analysis is to identify groups of objects that are very similar with regards to the input variables determined by the user (Sarstedt & Mooi, 2014). The similarity is determined by the log-likelihood distances calculated between the input variables. The input variables for this research included the post-stenting metrics described above (normalized TAWSS, normalized TAWSS variability and normalized WSSET). This research specifically used the two-step clustering method in the SPSS statistical software. Two-step clustering is a combination of hierarchical and partitioning (k-means) clustering methodologies (Sarstedt & Mooi, 2014). Two-step clustering was initially chosen because it allowed for the inclusion of mixed variables (categorical and continuous). However in the final analysis, the two-step clustering approach included only three post-stenting continuous input variables listed above, to see if a predictive metric could be determined to have a relationship to NT. Another benefit of this two-step cluster approach, as compared to traditional clustering methods, is that the optimal number of clusters is determined automatically through the second step of this two-step approach (Chiu et al., 2001). This ability avoids user input and the associated error in prescribing the number of clusters in this statistical approach.

The three continuous variables included as the only inputs for the cluster analysis were mean normalized TAWSS, variability normalized TAWSS and mean normalized WSSET. Evaluation fields, which are the variables in the cluster data that are not included as inputs for cluster analysis, were displayed for all other variables associated with each OCT slice. The only evaluation field that was a continuous variable was the CLA metric described earlier. The categorical variables displayed as evaluation fields were the stent types, drug-elution agent, vessel

location and diabetic status. The final categorical variable included in the cluster analysis is an indication of whether no malapposition occurred between stent and lumen contours at the follow-up OCT (=0), whether malapposition occurred between stent and lumen contours at the follow-up OCT (=1), whether uncovered stents were marked at follow-up (=2), or whether malapposed struts were marked at follow-up (=3). Figure 25 shows examples of the labeling of these categorical variables on follow-up OCT images.

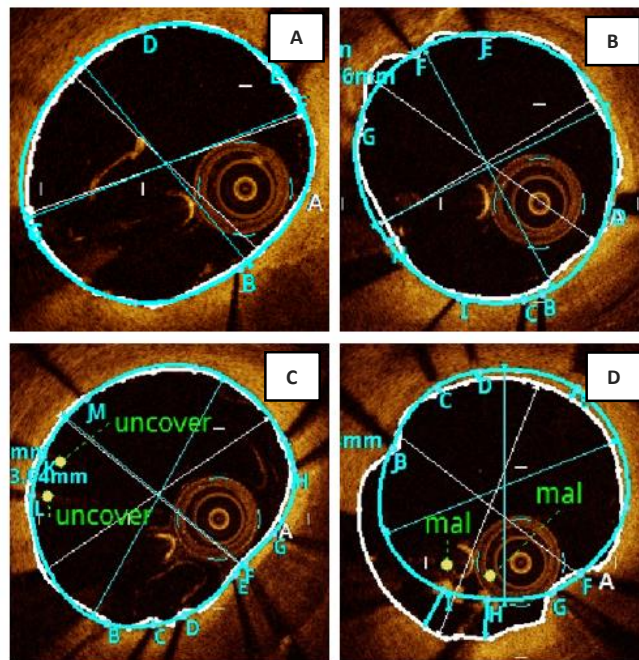


Figure 25: Follow-up OCT labeling. White and teal contours corresponds with lumen and stent locations, respectively. Follow-up images without regions of malapposition (A), with regions of malapposition (B), with marked uncovered struts (C), and with marked malapposed struts (D) were designated with 0, 1, 2, and 3 categorical labels, respectively.

The remaining variables, categorical or continuous, were then be used as evaluation fields and are simply markers showing the groupings of the variables that were included in the cluster analysis.

Chapter 3

Results

3.1 Aim 1: Local Analyses of a Case with Both Positive and Negative CLA

To target Aim 1, a single case (Case 5046) was selected that had OCT slices along the vessel length that included both negative CLA and positive CLA. Values for traditional post-stenting CFD metrics (mean normalized TAWSS and mean OSI) as well as recently proposed post-stenting CFD metrics (normalized TAWSS variability and mean WSSET) were calculated for slices that showed the largest positive and largest negative CLA.

The analyzed local results were of the slice with the largest negative CLA. This represents NT as seen in the image pair shown in Figure 26 below.

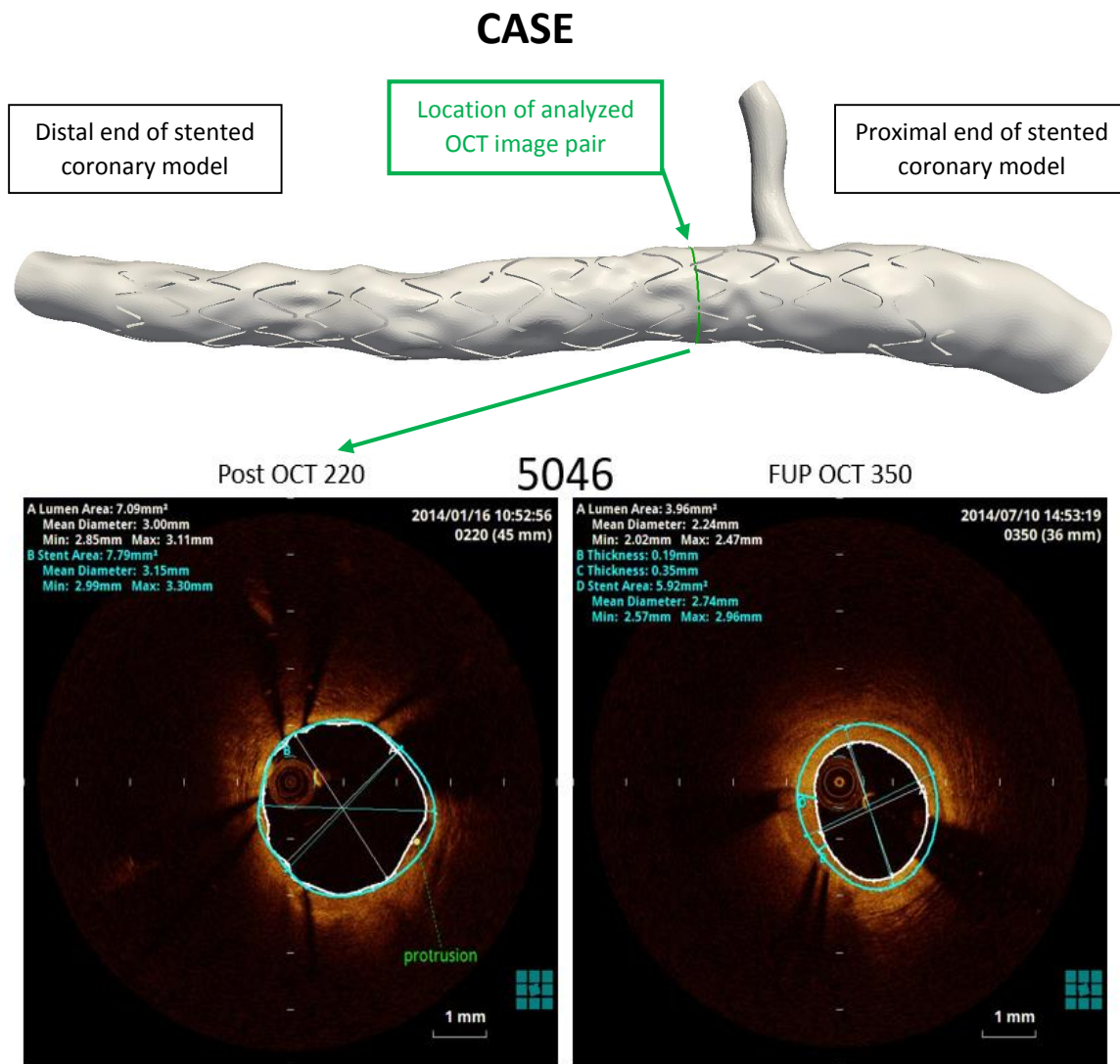


Figure 26: Post-stenting case with an OCT slice pair showing the largest negative CLA in the stented region. Green slice on the model is the location of the OCT slice 220 shown above. Corresponding follow-up OCT 350 is shown to describe the CLA of a -44.1% decrease. Local analysis of post-stenting metrics for an image pair showing a negative CLA from post to 9-months follow-up.

Traditional post-stenting metrics were calculated at the OCT slice shown in Figure 26 and were 1.33 and 0.07 for mean normalized TAWSS and mean OSI, respectively.

All 30 OCT slice pairs in this case are shown as the blue line going from the distal end (left) to the proximal end (right) in the stented region. The green vertical line represents the slice with the largest negative CLA (-44.1%). The collection of slices can be seen in Figure 27.

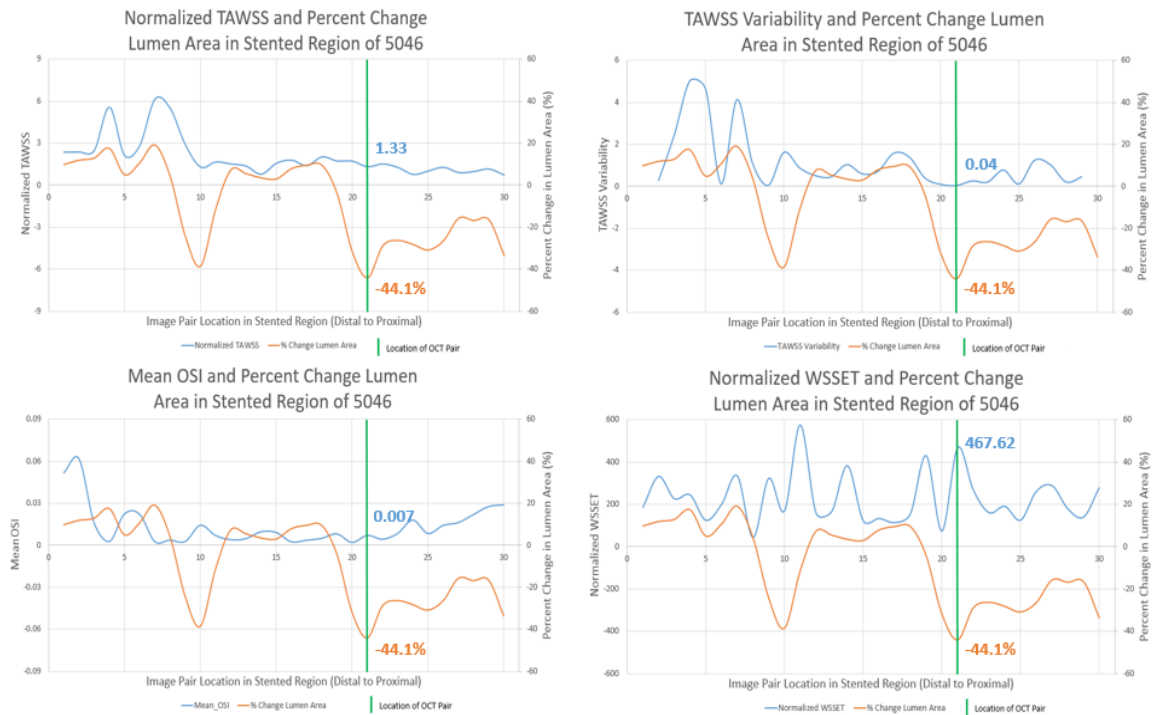


Figure 27: Stented image pairs plotting traditional WSS metrics (Normalized TAWSS on the top left; Mean OSI on the bottom left) and recent WSS metrics (TAWSS variability on the top right; Mean WSSET on the bottom right) shown in blue and each image pair's CLA shown in orange. Vertical green line indicates location of largest negative CLA for Case 5046 (Figure 26).

Recently proposed post-stenting metrics were calculated at the OCT slice shown in Figure 27 and were 0.04 and 467.62 for normalized TAWSS variability and mean WSSET, respectively. All 30 OCT slice pairs in this case are shown as the blue line going from the distal end (left) to the proximal end (right) in the stented region. The green vertical line represents the slice with the largest negative CLA (-44.1%).

The largest positive CLA for the selected case (5046) can be seen in Figure 28.

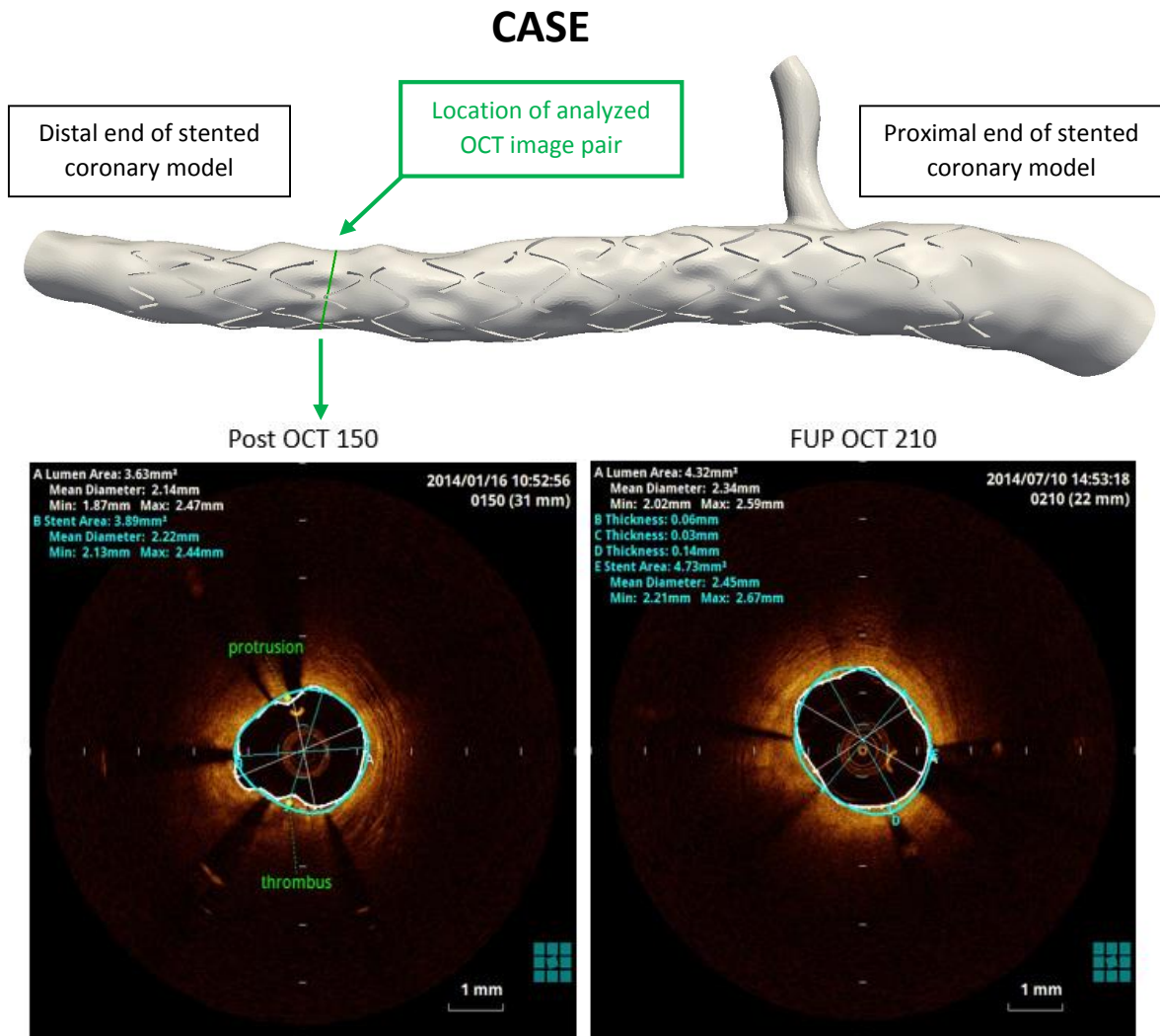


Figure 28: Post-stenting case with an OCT slice pair showing the largest positive CLA in the stented region. Green slice on the model is the location of the OCT slice 150 shown above. Corresponding follow-up OCT 210 is shown to describe the positive CLA of +19.0% increase. Local analysis of post-stenting metrics for an image pair showing a positive CLA from post to 9-months follow-up.

Traditional post-stenting metrics were calculated at the OCT slice shown in Figure 28 and were 6.14 and 0.03 for mean normalized TAWSS and mean OSI, respectively. All 30 OCT slice pairs in this case are shown as the blue line going from the distal end (left) to the proximal

end (right) in the stented region. The green vertical line represents the slice with the largest positive CLA (+19.0%). The collection of slices can be seen in Figure 29.

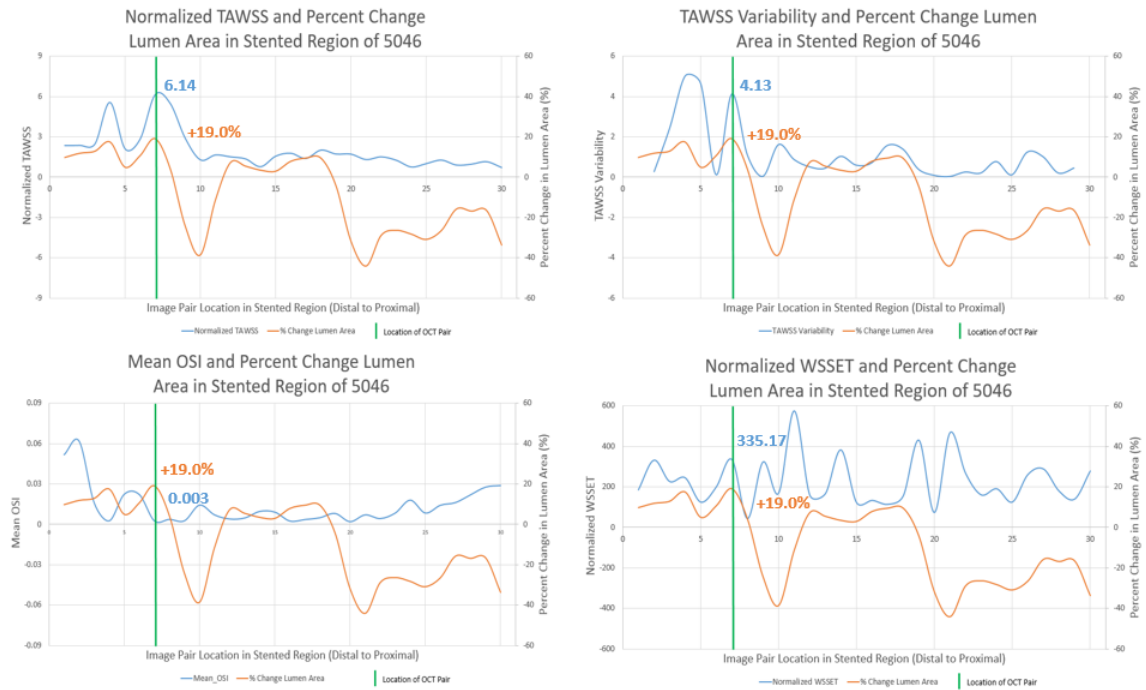


Figure 29: Stented image pairs plotting traditional WSS metrics (Normalized TAWSS on the top left; Mean OSI on the bottom left) and recent WSS metrics (TAWSS variability on the top right; Mean WSSET on the bottom right) shown in blue and each image pair's CLA shown in orange. Vertical green line indicates location of largest positive CLA for this Case (Figure 28).

Recently proposed post-stenting metrics were calculated at the OCT slice shown in Figure 29 and were 4.13 and 335.17 for normalized TAWSS variability and mean WSSET, respectively. All 30 OCT slice pairs in this case are shown as the blue line going from the distal end (left) to the proximal end (right) in the stented region. The green vertical line represents the slice with the largest positive CLA (+19.0%).

Table 3: Summary of post-stenting metrics quantified for case 5046 inspecting OCT image pairs with the largest negative CLA (-44.1%) and the largest positive CLA (+19.0%).

Case 5046		
Post-stenting Metric		% Δ LA Post to Follow-up
Mean normalized TAWSS	1.33	-44.10%
Mean OSI	0.007	
Variability TAWSS	0.04	
Mean normalized WSSET	476.62	
Mean normalized TAWSS	6.14	19.00%
Mean OSI	0.003	
Variability TAWSS	4.13	
Mean normalized WSSET	335.17	

Mean normalized TAWSS for the slice with the largest negative CLA (indicating restenosis) was 1.33. This metric increased to 6.14 for the slice with the largest positive CLA (indicating resorption). Similarly, the variability of TAWSS for the slice with the largest negative CLA was 0.04. This metric increased to 4.13 for the slice with the largest positive CLA. These results suggest that low values of normalized TAWSS and normalized TAWSS variability may be associated with sites of restenosis and high values of normalized TAWSS and normalized TAWSS variability may be associated with sites of resorption.

Mean normalized WSSET for the slice with the largest negative CLA was 476.62. This metric decreased to 335.17 for the slice with the largest positive CLA. These results suggest that high values of normalized WSSET may be associated with sites of restenosis and low values of normalized WSSET may be associated with sites of resorption.

Mean OSI for the slice with the largest negative CLA was 0.007. This metric decreased to 0.003 for the slice with the largest positive CLA. Although there is a change in the quantified OSI for the two locally analyzed slices, this difference is less than 10% of the overall range for all slices in this case. Due to this modest difference in the data relative to the other metric studied, mean OSI was not included in future data quantification.

3.2 Local Analyses Ranges of Quantified Post-Stenting Metrics from Aim 1

The results above suggest certain WSS indices may be predictive of restenosis or resorption. In order to more fully evaluate the ability of traditional and recent WSS indices to predict NT or conversely, arterial resorption, after DES implantation, it is desirable to understand the range of data for all four post-stenting metrics across all slices in this study. In other words, do the trends shown above for case 5046 also present for all cases.

3.2.1 Local Analysis Example of Low vs High Normalized TAWSS

The first of the post-stenting metrics inspected was mean normalized TAWSS. Mean normalized TAWSS ranged from 0.11 to 6.14 across all quantified locally analyzed post-stenting slices. An example of local quantification for a case that included both low and with high normalized TAWSS can be seen in Figure 30:

Low Versus High Normalized TAWSS

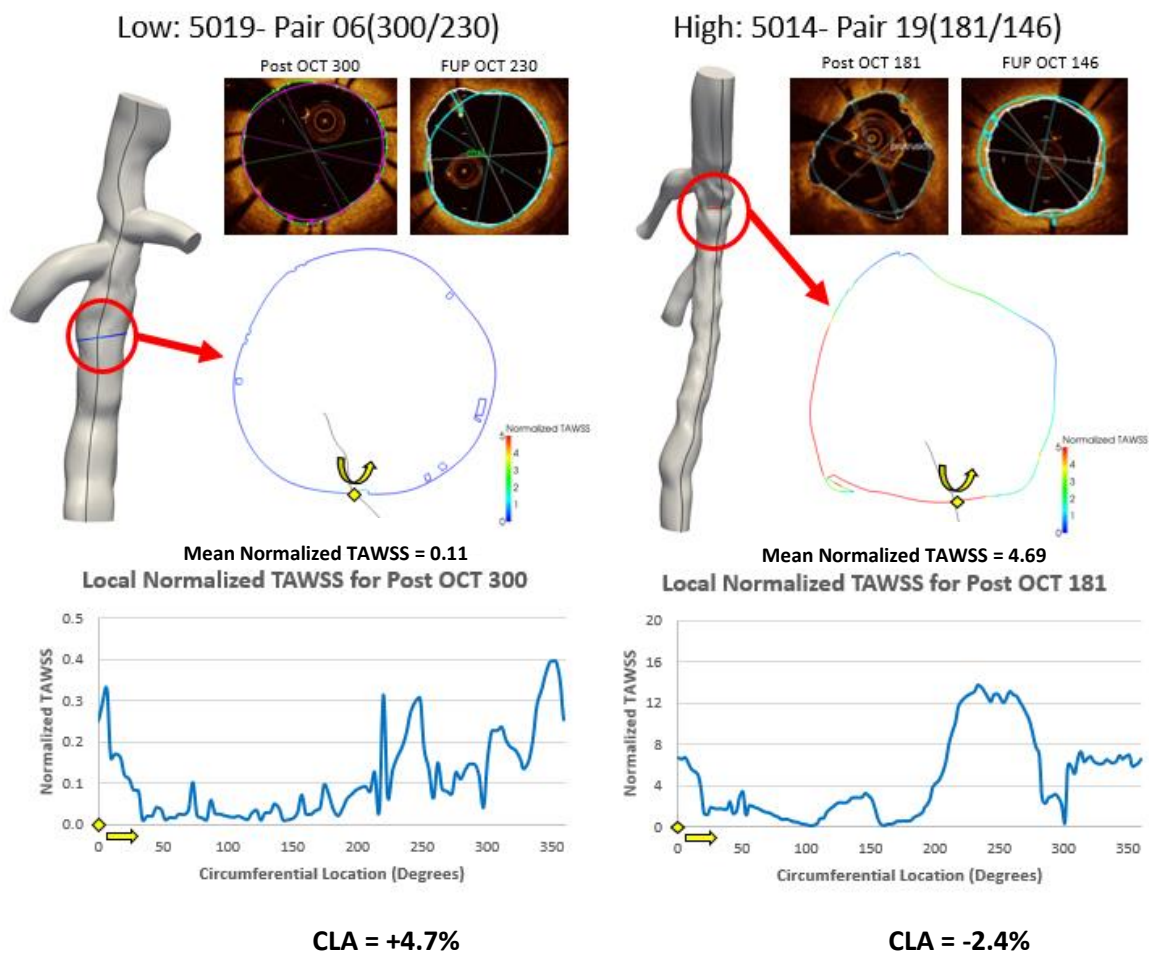


Figure 30: Local analysis of (a) low normalized TAWSS and (b) high normalized TAWSS

Figure 30 shows that a slice with a low mean normalized TAWSS (0.11) corresponds with a positive CLA (+4.7%) and that a slice with a high mean normalized TAWSS (4.69) corresponds with a negative CLA (-2.4%). Though these changes in lumen area are below 5% change for both examples, these local analyses contradict the findings from the Aim 1 results presented above, where low values of normalized TAWSS led to a decrease in lumen area and high values of normalized TAWSS led to an increase in lumen area. The ramifications and response to this contradiction will be discussed in more detail below, after the similar analyses that follows for other WSS indices.

3.2.2 Local Analysis Example of Low vs High Normalized TAWSS Variability

The second of the post-stenting metrics inspected was normalized TAWSS variability. Normalized TAWSS variability ranged from less than 0.01 to 6.04 across all quantified locally analyzed post-stenting slices. An example of local quantification for a case that included both low and with high normalized TAWSS can be seen in Figure 31:

Low Versus High Normalized TAWSS Variability

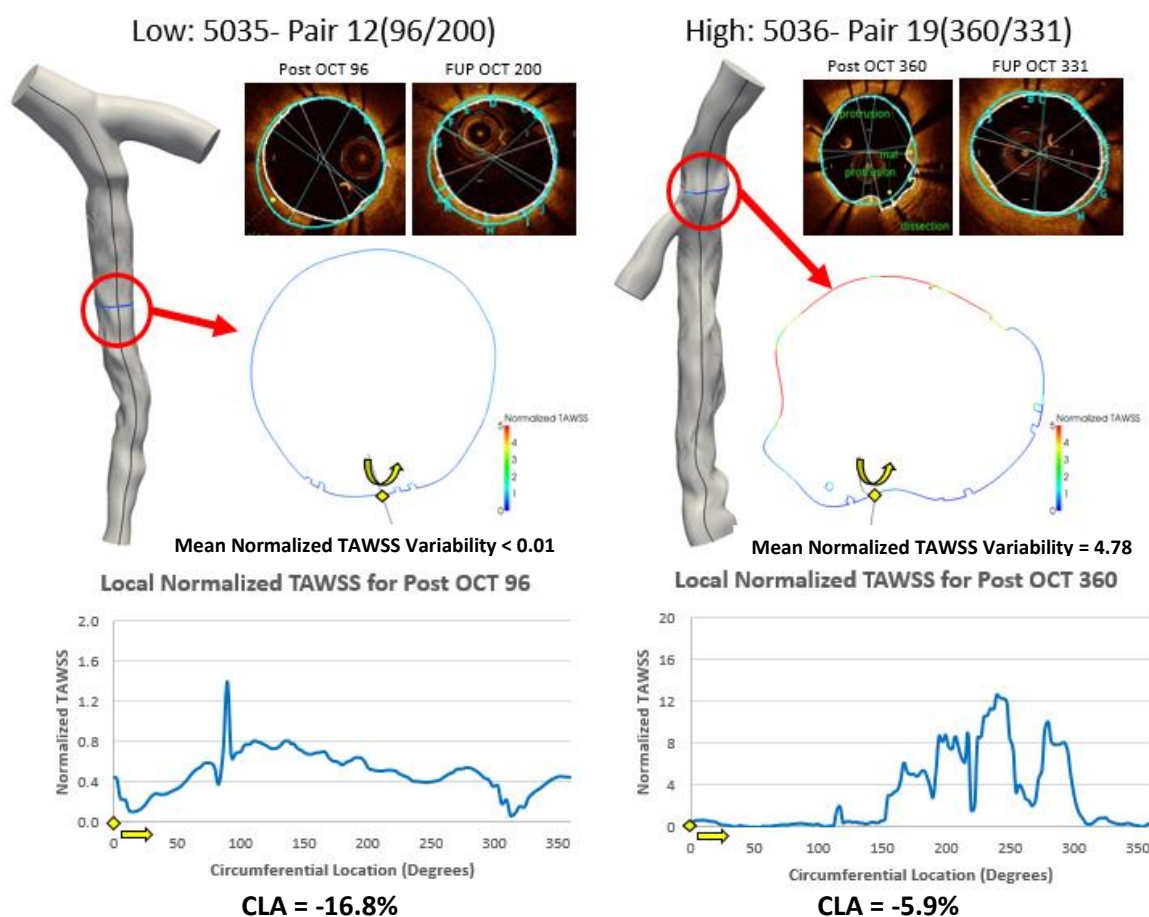


Figure 31: Local analysis of (a) low normalized TAWSS variability and (b) high normalized TAWSS variability

Figure 31 shows that a slice with a low normalized TAWSS variability (<0.01) corresponds with a negative CLA (-16.8%) and that a slice with a high normalized TAWSS variability (4.78) also corresponds with a negative CLA (-5.9%). These results show that high TAWSS variability is not predictive of resorption for all locally analyzed slices.

3.2.3 Local Analysis Example of Low vs High Normalized WSSET

The last of the post-stenting metrics inspected was mean normalized WSSET. Mean WSSET ranged from 1.25 to 952.08 across all quantified locally analyzed post-stenting slices. An example of local quantification for a case that included both low and with high mean WSSET can be seen in Figure 32:

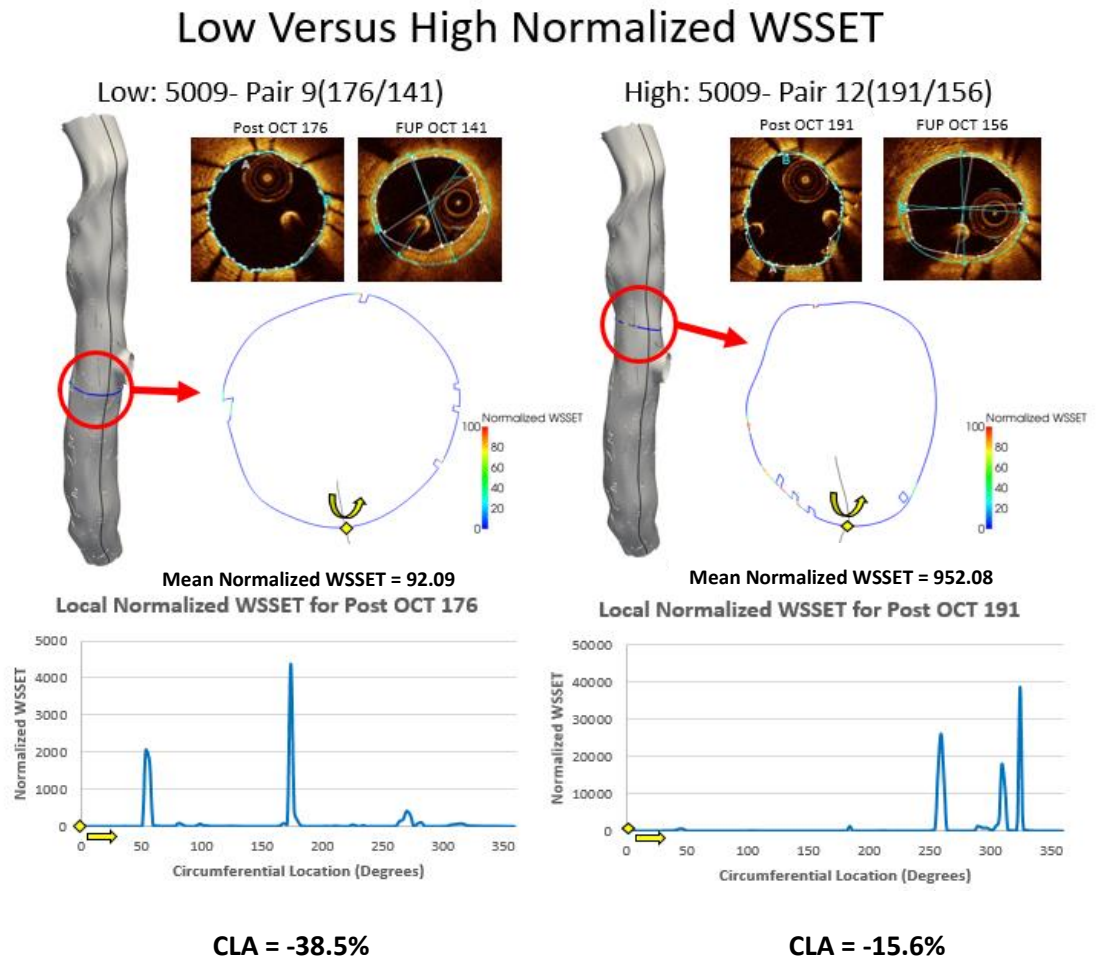


Figure 32: Local analysis of (a) low normalized TAWSS and (b) high normalized WSSET

Figure 32 shows that a slice with a low mean normalized WSSET (92.09) corresponds with a negative CLA (-38.5%) and that a slice with a high mean normalized WSSET (952.08) also corresponds with a negative CLA (-15.6%). These local analyses contradict the findings in

Aim 1 Results that high values of mean normalized WSSET may be associated with restenosis and low values of mean normalized WSSET may be associated with resorption.

Aim 1 results show the metrics from a single case are not predictive of restenosis or resorption at the level of independent local analyses across all slices and cases. Therefore, cluster analysis of multiple local analyses is necessary to better understand the relationships between post-stenting metrics and restenosis or resorption.

3.3 Aim 2 Results: Two-Step Cluster Analysis for All Cases

3.3.1 Collection of Patient-Specific Post-Stenting Results

Post-stenting CFD results for normalized TAWSS and normalized WSSET for all cases can be seen in Figure 33. Normalized TAWSS variability was calculated from normalized TAWSS models. Normalized WSSET results do not include branches and other unstented portions of the model since they were not included in the quantification of all post-stenting metrics. A collection of 469 slices of post-stenting metrics were included across 29 patients in this analysis.

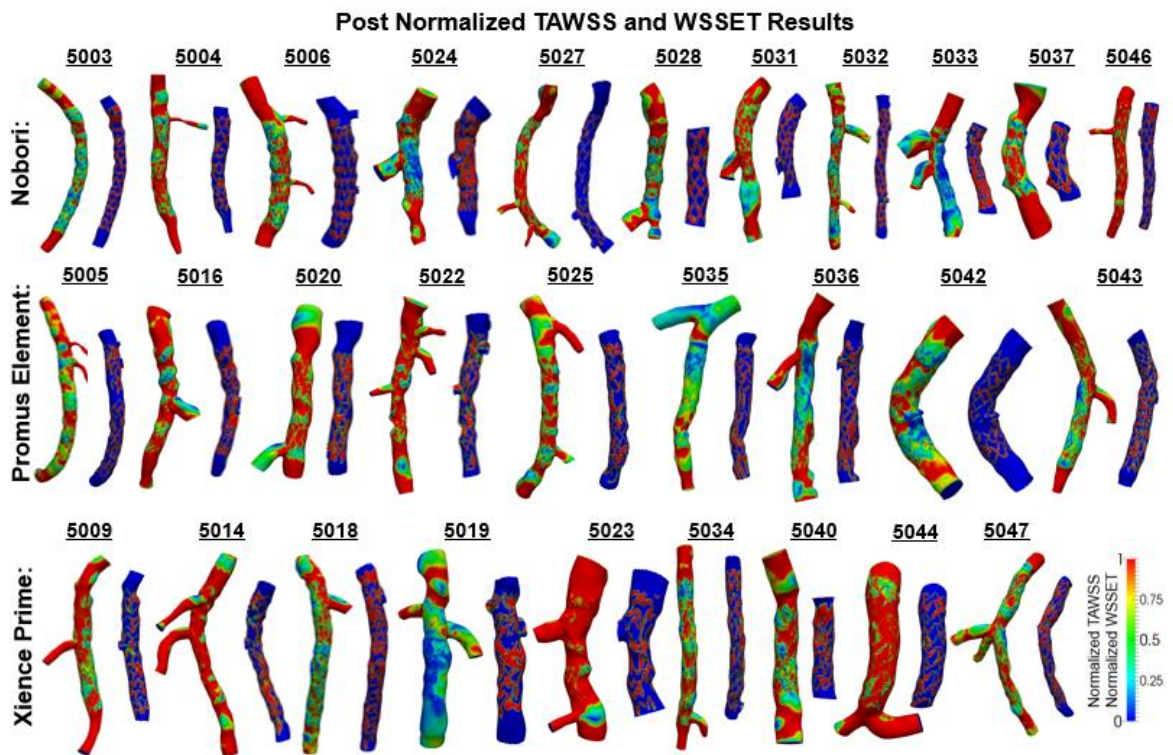


Figure 33: Post-stenting normalized TAWSS and WSSET results for 3 stent types evaluated.

3.3.2 Two-Step Cluster Analysis Summary

Two-step cluster analysis using three post-stenting metrics as inputs for all locally analyzed slices ($n = 469$) automatically grouped the slices into three clusters with the percentages of 58.8%, 18.8% and 22.4% for clusters 1, 2 and 3, respectively, as shown in Figure 34. Cluster quality measure produced a “good” value (>0.5) from this analysis. The silhouette measure of cohesion and separation, which is a measure of the clustering solution’s overall goodness-of-fit, is based on the average distance between objects and is between -1 and +1 (Sarstedt & Mooi, 2014).

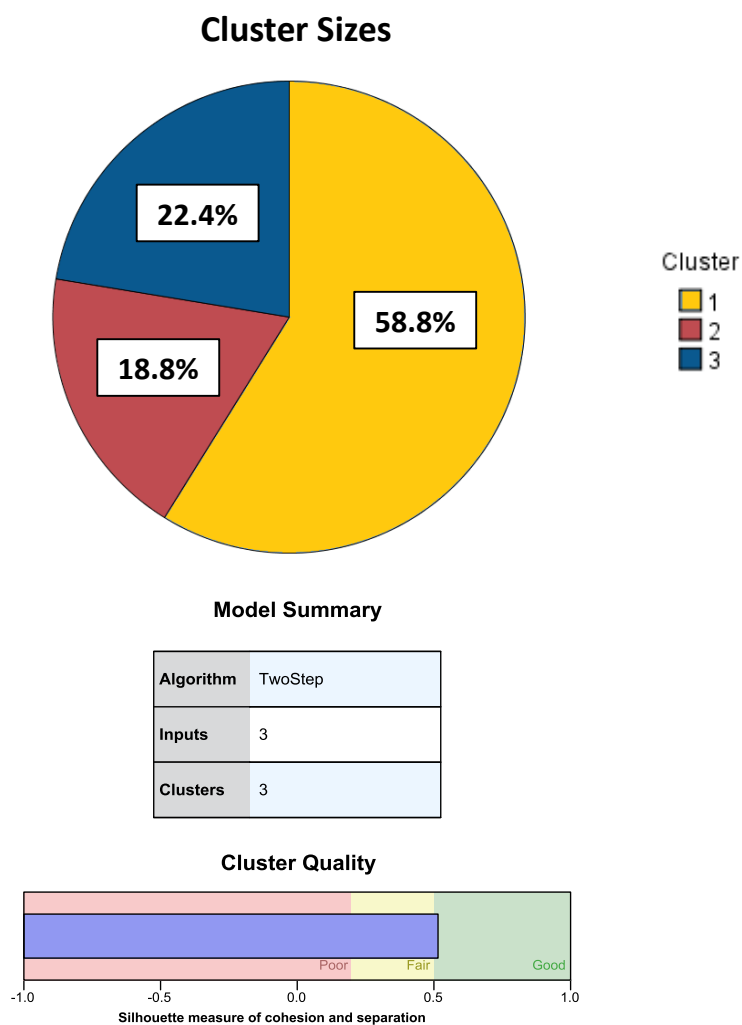


Figure 34: Two-step Cluster analysis results for 469 image pairs. Used 3 post-stenting metrics as inputs (Normalized TAWSS, Variability TAWSS, and Normalized WSSET) and produced 3 distinct clusters. SPSS software produced silhouette measure of cohesion and separation between the inputs indicating the cluster quality from this analysis falling in the “Good” range (>0.5).

3.3.3 Two-Step Cluster Analysis Absolute and Relative Distributions

The largest cluster (cluster 1: 58.8%) shows a composition of relatively low WSSET, TAWSS variability, and TAWSS values. The next largest cluster (cluster 3: 22.4%) shows a composition of relatively high WSSET and a composition of relatively low TAWSS variability and TAWSS values. All WSSET values >496 used in this study were automatically distributed to cluster 3. The smallest cluster (cluster 2: 18.8%) shows a composition of relatively low WSSET and a composition of relatively high TAWSS variability and TAWSS values. All TAWSS variability values >2.48 and TAWSS values >2.28 used in this study were automatically distributed to cluster 2. A summary of the cluster results is shown in Figure 35.

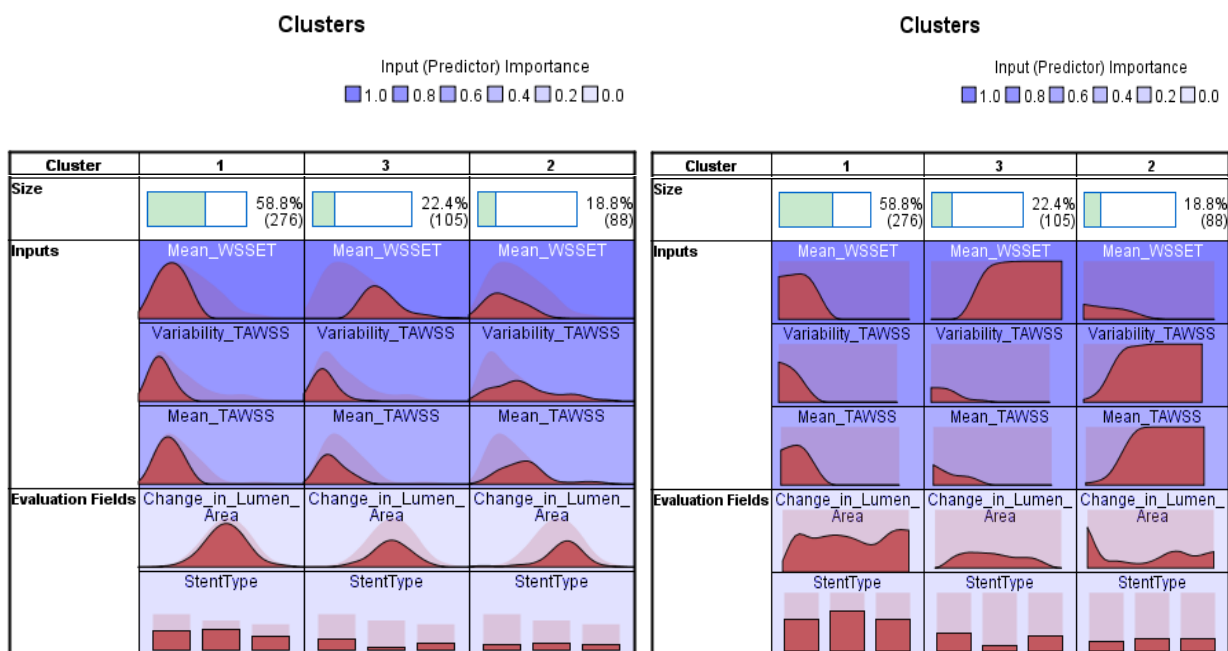


Figure 35: Absolute (left) and relative (right) distributions of 3 cluster output produce from two-step cluster analysis. Clusters are in order from left to right with respect to the cluster sizes.

Inputs are sorted from top to bottom with respect to their “predictor importance” measure produced by SPSS indicating the significance of each input: Mean WSSET (predictor importance = 1.00), TAWSS Variability (predictor importance = 0.77), and Mean TAWSS (predictor importance = 0.56). Evaluation Fields report the absolute and relative distributions of the CLA measure and the stent type (Nobori-left bar, Promus-middle bar, Xience-right bar). WSSET values > 496 only present in cluster 3. TAWSS variability values > 2.48 and mean TAWSS values > 2.28 only present in cluster 2.

3.3.4 Two-Step Cluster Comparison of Three Output Clusters

Overall and individual cluster (three-cluster output) distributions for each post-stenting metric are presented in Figure 36. SPSS Software provided median values for these distributions and corresponding lower and upper quantiles (left and right edge of white box for overall quantiles and left and right points of lines for each cluster) for each distribution (25% and 75% quantiles).

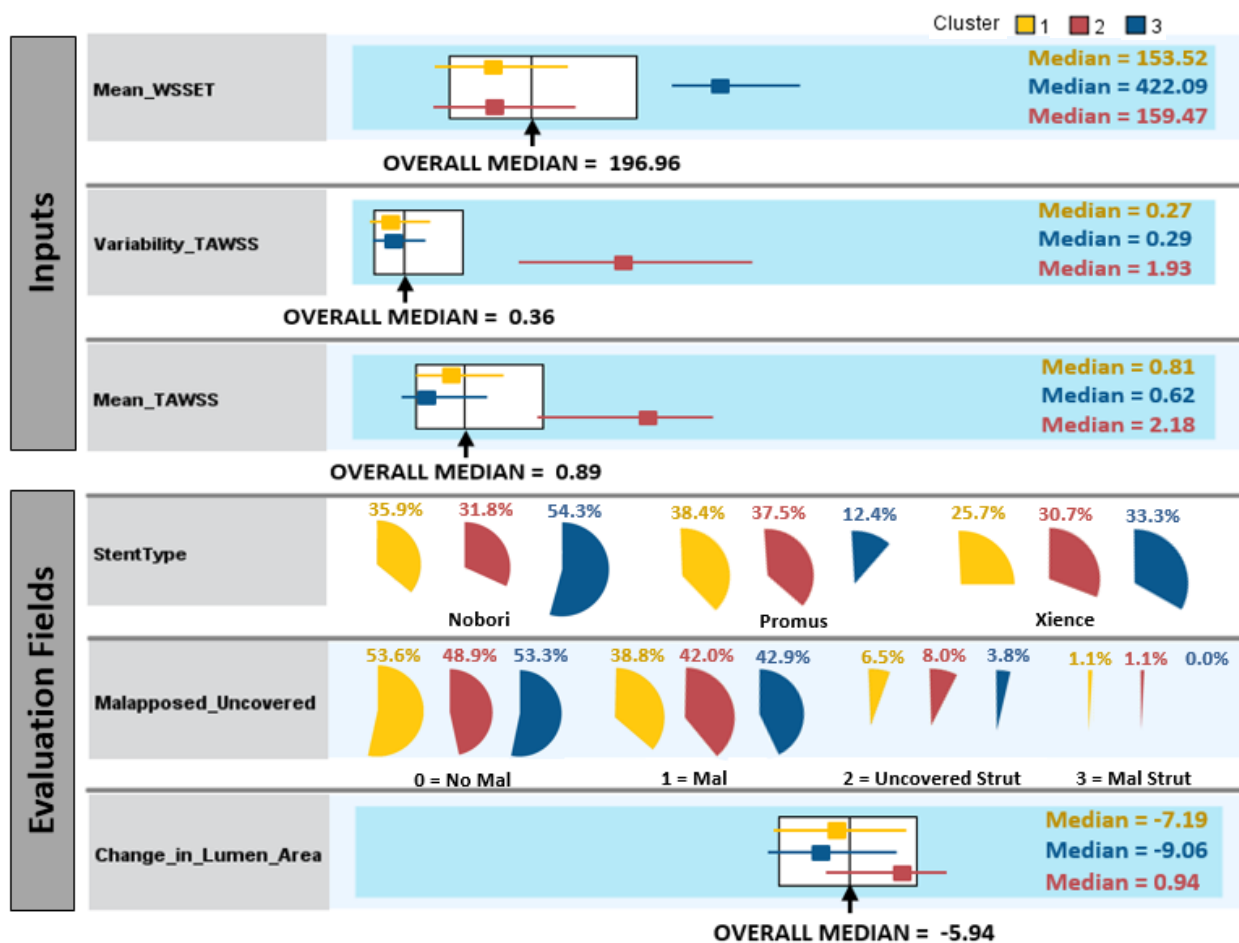


Figure 36: Cluster Analysis output presenting the distributions of the three post-stenting metric inputs and their corresponding three evaluation fields (stent type, follow-up OCT labeling, and CLA). White boxes show the overall distributions of the three post-stenting and one follow-up continuous variables indicating the overall median for all 469 analyzed image pairs. The left and right ends of the white boxes indicate the lower quartile and upper quartile of the overall data set as well. Colored boxes indicate the medians of each cluster along with the lines representing the lower and upper quartiles of each cluster output.

Cluster 1 post-stenting metrics all conveyed medians within the quantiles of the overall distribution of data leading to a CLA median (-7.19) closest to the overall CLA median (-5.94). Cluster 2 consisted of 2 post-stenting metrics (Mean TAWSS and Variability TAWSS) with medians above the 75% overall quantile for each metric which led to a CLA median of 0.94, indicating an increase in lumen area (resorption) compared to the overall median value of -5.94. Cluster 3 consisted of 1 post-stenting metric (Mean WSSET) with a median above the 75% overall quantile for the WSSET metric which led to the largest negative CLA median of -9.06 (restenosis). Cluster 3 also exhibited the lowest median for the mean TAWSS metric (0.62) which led to the largest negative CLA median (restenosis).

Cluster 3 contained the largest frequency of Nobori types (54.3%) compared to Clusters 1 and 2. Clusters 1 and 2 had a more even distribution of the 3 stent types with the largest frequency of the Promus stent with 38.4% and 37.5% in Cluster 1 and Cluster 2, respectively.

Cluster 3 contained the smallest frequency of follow-up OCT images marked uncovered struts (3.8%), or marked malapposed struts (0.0%) compared to Clusters 1 and 2. Cluster 2 contained the largest frequency of follow-up OCT images with malapposition, marked uncovered struts, or marked malapposed struts ($100\% - 48.9\% = 51.1\%$) compared to Clusters 1 and 3.

Chapter 4

Discussion

4.1 Overview of Aims and Summary of Major Findings

The overall objective of this study was to describe how WSS and its derivatives affect restenosis and resorption. This objective is important because the cause of coronary artery NT leading to restenosis in ~10% of DES is still unknown and even less is known about resorption (Hughey, 2014). Prior studies comparing TAWSS to restenosis for first generation DES yielded conflicting results and cited different mechanisms of action for DES agents (Gijssen et al., 2003; Papafaklis et al., 2010; Suzuki et al., 2008). Recent research on second generation DES made significant contributions in the geometrical representation of patient-specific coronary models and in quantifying WSS metrics from those models. For example, Gundert et al performed CFD simulations on idealized stented coronary arteries to create a hierarchy of stent design factors that can result in adverse WSS distributions. The authors found that strut thickness had the greatest impact on adverse WSS distributions (Gundert et al., 2012). Gundert et al used TAWSS and OSI, traditional WSS indices, to find those correlations between stent geometry and local distribution of adverse WSS, correlating with NT. Hughey et al also analyzed TAWSS and OSI, but using patient-specific stented coronary models. The models incorporated malapposed stent struts, affecting WSS on the vessel wall behind the free-floating struts (Hughey, 2014). That research primarily focused on regional analyses, where areas of WSS values below a certain threshold were identified and correlated to NT. While Hughey et al also performed local analyses, the three local results were selected by the user and did not omit stent struts in their quantification (Hughey, 2014).

The results presented in this thesis build on the previous work discussed above, but differ in that new WSS metrics (WSS variability and WSSET) are included in the analyses. Also, the

methodology of this thesis avoided selection by the user by including all locally analyses available in the stented region, making it more reliable and unbiased. The results show that independent local analysis of post-stenting metrics is not sufficient to predict restenosis or resorption outcomes in stented coronary arteries. The complete inclusion of multiple local analyses through the use of cluster analysis is a more appropriate approach to truly understand the relationship between post-stenting metrics and restenosis or resorption. The use of cluster analysis allows for the local level to be quantified, while uncovering the potential predictive relationships contributing to restenosis or resorption across hundreds of locally analyzed slices. Perhaps most importantly, this research also showed that predicting restenosis or resorption is best accomplished through a combination of multiple post-stenting metrics. Collectively, the current results suggest high normalized TAWSS in combination with high normalized TAWSS variability may be associated with resorption, while high normalized WSSET in combination with low normalized TAWSS may be associated with restenosis.

4.2 Review of Findings from Aim 1: Local Relationship of Traditional and Recent WSS Indices to NT and Vessel Resorption

The first specific aim in pursuing the objective of this research was to evaluate the ability of traditional and recently-developed WSS indices locally, and determine their ability to predict NT, or conversely, resorption after DES implantation. For this aim, one stented coronary artery was selected based on it having marked regions of a positive CLA for a given post-stenting to nine-month follow-up image pair, as well as a negative CLA for a given image pair in the same model. The largest positive CLA suggests resorption of the vessel wall and a negative CLA suggests restenosis of vessel wall at the local level of each OCT pairing. Moreover, these different reactions of the vessel wall underline the importance of the local analysis of post-stenting metrics at those given locations.

The first locally analyzed pair showing a marked negative CLA can be seen in Figures 26 and 27. For this image pair, a marked negative CLA of -44.0% can be seen in Figure 27 with relatively low normalized TAWSS and TAWSS variability post-stent metrics, and a relatively high WSSET post-stenting metric. The measured larger value of WSSET appears to be correlated the negative CLA; however, this finding is based on only one analyzed image pairing and is therefore not sufficient to provide any conclusions.

In the comparison of traditional post-stenting metrics with the recently-proposed metrics in Figure 27, it was challenging to identify specific metrics of correlation to a CLA value. At the location of the image pair presented in Figure 26, marked by the green vertical line in Figure 27, only the WSSET showed a local maximum value, while mean TAWSS, mean OSI, and TAWSS variability metrics showed no change relative to proximal and distal pairs. A larger WSSET value indicates a local region of greater accumulated time of WSS vectors over the cardiac cycle, which may represent a local region of stagnant blood, leading to the blood vessel being allowed to undergo NT. Furthermore, the locally analyzed slice showed values of relatively low normalized

TAWSS (1.33), shown by previous research done by Hughey et al as well as others, leads to restenosis at follow-up (Hughey, 2014; Murphy & Boyle, 2010; Van Der Heiden et al., 2013). Murphy et al reported that EC subjected to low WSS (<0.5 Pa) are circular in shape and have no preferred alignment pattern (Murphy & Boyle, 2010). This feature coupled with the blood stagnation typically seen in areas of low WSS leads to an “increase uptake of blood borne particle to the artery wall as a result of increased residence time and increase permeability of the endothelial layer” leading to tissue growth (Murphy & Boyle, 2010). A combination of the traditional post-stenting metric of normalized TAWSS, coupled with the recently developed post-stenting metric of WSSET, may be indicative of NT formation at follow-up. However, as previously mentioned, one locally analyzed region is not sufficient to justify the overall reactionary behavior of the vessel wall.

The second locally analyzed pair showing a marked positive CLA can be seen in Figures 28 and 29. For this image pair, a marked positive CLA of +19.0% can be seen in Figure 28 with relatively high normalized TAWSS and TAWSS variability post-stent metrics and, interestingly, a relatively high WSSET post-stenting metric compared to the overall dataset (Figure 29). For this locally analyzed pair showing an opposite reaction to the first locally analyzed pair, the fundamental behavior of arteries should be addressed. For example Dolan et al described the adaptive response of an artery to chronically elevated high flow. “The function of an artery to maintain a WSS baseline appears to ensure that the metabolic needs of tissues are met while energy loss due to friction is minimized” (Dolan et al., 2013). Specifically, the adaptive response of an artery to a chronically elevated high flow is that it undergoes expansive or outward remodeling to restore WSS back to baseline levels (Dolan et al., 2013). Dolan et al reported that “recent advances in intracranial aneurysms (IA) pathogenesis using animal models have shed light on the role of high WSS in pathological remodeling, pointing to high WSS in combination with positive WSSG along the flow direction as the hemodynamic trigger for IA formation”

(Dolan et al., 2013). In the current study, WSS variability is a post-stenting metric quantified to represent the changing WSS distribution collectively from one locally analyzed slice to the next. The marked relatively high values in both normalized TAWSS as well as TAWSS variability for the locally analyzed image pair, showing positive CLA in Figure 31, corresponds with this trend of positive remodeling shown by Dolan et al. A relatively high value of WSSET was quantified for this image pair showing resorption, which may indicate that a high WSSET needs to be coupled with low TAWSS to initiate NT, as shown in Figure 29. Further comparisons with proximal and distal image pairs of traditional post-stenting metrics as well as recently created post-stenting metrics for this image pair in Figure 29, shows that resorption can be seen in other locations within the stented region. However, as mentioned earlier, the independent local analysis cannot define the overall reactionary behavior of the vessel wall.

In order to better understand the local analyses performed targeting Aim 1, the range of data for each post-stenting metric was analyzed at the local level. Specific locations corresponding with low and high calculated normalized TAWSS averages were shown in Figure 30. The example presenting the low normalized TAWSS has different characteristics compared to its counterpart presented in Figure 30. The low TAWSS local analysis on the left side of Figure 30 has a vessel shape that is more circular compared to the rectangular shape shown in the vessel with high normalized TAWSS shown on the right. This difference in vascular shape presumably leads to differences in the imposed WSS distribution on the vessel wall. The post OCT image of the rectangular cross section with the high normalized TAWSS has the label of a protrusion in the OCT image as labeled by the cardiologist. Bends, undulations and bifurcations in the vasculature change the distribution of WSS and are therefore important considerations in the analysis.

Specific stent geometries led to altered distributions of WSS on the vessel wall. Gundert et al. investigated how reducing the number of circumferentially repeating crowns, or peaks, in the stent geometry for current stents may improve the hemodynamic environment within stented

arteries and reduce the likelihood of excessive neointimal growth and thrombus formation (Chiastra et al., 2016). The specific stent designs investigated for this study directly affected the measured normalized TAWSS distribution on the vessel wall. At the local level, the presence of the stent struts may vary substantially, even within the same stent geometry, based on the orientation and placement of the local analysis plane corresponding to the OCT image provided. The Nobori stent is symmetric and periodic, and is of the peak-to-peak stent type. The Promus and Xience stent types are asymmetric and are of the peak-to-valley stent type. Also, the Xience stent has extendable connectors that further influence the contribution of the stent geometry to the distribution of WSS on the vessel wall.

Defining how the stent is interacting with the vessel wall is essential to understanding how traditional and recent WSS indices vary and behave. For example, Figure 30 shows the marked differences in mean normalized TAWSS. Stent struts are shown to be free-floating (i.e. malapposed), which led to adverse WSS behind the struts, resulting in the measured low average presented in Figure 30. Contrasting this was the rectangular vessel with minimal malapposed stent struts present, which did not have many regions of low WSS, giving the mean WSS a larger calculated value. Therefore, it is crucial to recreate as accurately as possible the orientation of the stent within the vessel since strut orientation may determine whether or not a stent becomes malapposed.

A recent approach to characterizing the WSS distribution on the vessel wall is through the determination of the WSS variability, using the in-house algorithm proposed in this study. This method of analyzing variability characterizes the changes in WSS distributions circumferentially as well as longitudinally. Examples of low and high variability can be seen in Figure 31. Similar to the measure of mean normalized TAWSS in Figure 30, normalized TAWSS variability shows how a vessel with many malapposed struts combined with large vascular geometrical perturbations may be associated with the larger measured TAWSS variability value.

The novel contribution of this index is the awareness that calculating the variability in a local slice is not simply a measure of the variability of WSS for that plane, but also is a measure of variability between the proximally and distally analyzed cross sections by way of the second derivative. An idealized vessel with a narrowing does not change in longitudinal TAWSS variability from cross section to cross section, indicating that this approach underscores circumferential variability due to factors described above.

Another recent approach to characterize the distribution of WSS values is the quantification of WSSET. Local examples of low and high normalized WSSET can be seen in Figure 32. This index is a measure of the accumulation of WSS vectors pointing to specific locations on the vessel wall over the cardiac cycle. The WSSET metric is measured in units of normalized cardiac cycle periods. The larger the normalized WSSET value, the longer amount of accumulated time all of the WSS trajectories in the boundary layer are visiting a given surface element of the discretized model. In observing regions of high accumulation of trajectories (or a higher measured WSSET value) in Figure 32, one can see that larger values are present between struts. Therefore, when more cross-sectional struts are present in a given analyzed OCT slice, one would see a larger measured WSSET value measured for that slice. Opposite to this, where there are fewer struts present in the OCT slice, one would see a smaller measured WSSET value. Furthermore, since WSS trajectories may be coming from regions proximal or distal to the analyzed localized plane, this local analysis is specific to the analyzed OCT image plane. Arzani et al developed this metric and analyzed it on abdominal aortic aneurysms (Arzani et al., 2016a). From the simulated results in that study, it was concluded that WSSET can “provide a template for near-wall transport,” which is especially relevant for DES compared to BMS since the drug-elution process is occurring in conjunction with the altered hemodynamics present from the stent geometry (Arzani et al., 2016a). This is the first study to date that used this post-stenting metric in the analysis of stented coronary arteries.

In summary, in targeting Aim 1, the measured post-stenting metrics showed similar trends at the local level with previous research (Hughey, 2014). However, the addition of several new post-stenting metrics showed more promise than one metric leading to a specific outcome at the local level. To validate overall reactionary behavior of the vessel wall as measures of the quantified post-stenting metric (or a combination of metrics), a more collective analysis needed to be performed as part of Aim 2.

4.3 Review of Findings from Aim 2: Cluster Analysis Significance

The second specific aim was addressed by using cluster analysis to uncover which stent design and/or patient-specific attributes correlate with NT or vessel resorption using complex DES datasets (i.e. multiple continuous and categorical DES metrics) containing traditional and recent WSS indices. To collectively analyze the relationship of traditional and recent post-stenting metrics to the quantified CLA, and at follow-up, two-step cluster analysis was performed. With the three quantified post-stenting metrics described in Figures 30-32 used as inputs for this analysis, the two-step cluster automatically produced three output clusters shown in Figure 34. For the cluster analysis performed in this study, this measure of cohesion and separation between the clusters was at a “good” level (>0.5) and was provided by the SPSS software. With the cluster analysis producing good output, the overall histograms of the three distinct clusters can be analyzed.

The absolute and relative distributions of the output clusters can be seen in Figure 35. Cluster 3 showed a measured threshold of WSSET values where only values above 496 belonged to this cluster, while Cluster 2 claimed the threshold for TAWSS variability and TAWSS values of 2.48 and 2.28, respectively. The overall outcome of evaluation fields shown (stent type and CLA) is difficult to process in this view, which does not allow for easy appreciation of distributions within the evaluation fields.

Figure 36 reveals the overall distributions of this cluster analysis, which allows the user of to uncover factors contributing to restenosis or resorption from analyzing CLA in a way that spans locations and case. With the same reported clusters in Figures 34 and 35, Figure 36 reveals the relationship of the post-stenting metrics with the follow-up CLA. The overall median of all 469 analyzed image pairs in this study report the CLA as -5.94%. With a slight negative CLA being reported for the overall collection of image pairs, this indicates that the stented coronary

arteries undergo some NT, which is expected due to the nature of vascular injury the stent likely induced on the vessel. The largest cluster (gold; cluster 1) showed the closest median CLA (-7.19%) to the overall value.

Cluster 3 (blue) exhibited the lowest median CLA (-9.06%) indicating that this cluster showed the most restenotic behavior compared to the other two clusters. Furthermore, as previously seen in Figure 35, this cluster exhibited much higher median WSSET values (422.09) and slightly lower TAWSS median values (0.62) than the overall data values. The combination of these post-stenting metrics show restenotic behavior with the largest negative CLA.

Cluster 2 (red) exhibited the largest median CLA (+0.94%), indicating that this cluster showed the most resorption as compared to the other two clusters. Furthermore, as previously seen in Figure 35, this cluster exhibited much higher median TAWSS variability values (1.93) and much higher TAWSS median values (2.18) than the overall data values. The combination of these post-stenting metrics show resorption behavior with the largest positive CLA.

Furthermore, the Nobori stent type was the most prominent stent type for Cluster 3, the cluster showing the most restenotic behavior, accounting for 54.3% of the quantified image pairs compared to the other two stent types. This large percent of the quantified image pairs belonging to the Nobori stent type is likely due to the radial thickness of the stent struts leading to lower values of TAWSS as well as larger WSSET values. The marked threshold for WSSET (>496) for this cluster is the only definitive measure that may be predictive of restenosis.

Finally, the follow-up OCT labeling showed the lowest occurrence of no resorption (46.6%) for Cluster 2. This is another indication of how marked high values of TAWSS and TAWSS variability result in the most resorption properties as shown by Cluster 2. The marked threshold for TAWSS (>2.28) and TAWSS variability (>2.48) are the definitive measures from cluster analysis that may be predictive of resorption.

Drug-elution agent frequencies matched the stent types for each of the 3 DES investigated in this study. The biolimus-eluting Nobori stent had the largest frequency in Cluster 3 (54.3%) which led to the largest negative CLA (restenosis) while the everolimus-eluting Promus Element and Xience Prime stent types had the highest frequency in Cluster 1 (64.13%) and Cluster 2 (68.18%). With Cluster 2 having the largest positive CLA (resorption), this would indicate that the everolimus agent leads to more resorption properties than restenosis properties. However, since 2 of the 3 stents had the everolimus agent, it should be recognized that there were more inputs weighting the results towards the everolimus drug-elution agent. Also, mechanical factors may play a more substantial role in characterizing the measured post-stenting metrics.

Patients with diabetes have noted smaller coronary arteries, where a coronary stent may be more likely to undergo restenosis as compared to a larger artery. Diabetic status in this research did not appear to have a relationship to restenosis or resorption. This was characterized by the even distribution of patients with diabetes across all 3 clusters. Cluster 1, 2 and 3 each had 53.26%, 51.14% and 47.62% of patients with diabetes respectively. Current research has shown that the selection of specific drug-eluting stents for diabetic patients is controversial (Stefanini & Holmes, 2013), which is consistent with the findings of this research.

The results show promise for clinical application in the predictive capabilities of local stent-induced WSS metrics (both traditional and recently proposed) and their relation to unfavorable follow-up outcomes (restenosis or vessel resorption). First, the combination of traditional and recently proposed metrics is more effective in showing a relationship to restenosis or resorption than isolated WSS metrics. With these metrics, a physician would be able to locally identify areas of concern where the WSS metrics reside outside the normal ranges. This ability to monitor the stent-induced reaction of the vessel wall in potentially problematic patients would be valuable in the clinical setting. Second, this research shows that there is a potential relationship between a combination of high TAWSS (>2.28) and high TAWSS variability (>2.48) with vessel

resorption. This finding is important clinically because it may be used to indicate complications in individual patients, such as thrombosis. Third, high values of WSSET (>496) combined with low WSS exhibit a potential relationship with restenosis. This is clinically important because WSSET has not been quantified for stented coronary arteries and could be revealing of NT formation, causing restenosis. Finally, the collection of a variety of analyzed slices from different branches of the coronary tree, along with the use of three different stent types, provides a more realistic perspective of the diverse clinical setting. A wide range of analyzed CFD results provides more clinical significance to the WSS metrics and their potential relationship to restenosis or resorption.

4.4 Limitations and Future Directions

These encouraging results should be interpreted within the constraints of several potential limitations. Firstly, patient-specific models were assumed to be rigid. Physiologically, this is not true for the coronary arteries, as there is some compliance in the vessel wall that shows distensible properties over the cardiac cycle, even though the stents region was previously found to be largely rigid after balloon-expandable stent implantation (LaDisa Jr. et al., 2002). Furthermore, the vessel wall was not modeled, which means the variable structural properties of the coronary arteries consisting of an assortment of coronary tissues (healthy tissue, plaques, thrombus, NT, etc.) were not able to impact local deformation of the stent during some FEA simulation. While the Boolean approach is able to capture local geometric perturbations, and local tissue properties were not available for use in FEA as we have done previously (Chiastra et al., 2016), this methodological choice can still be seen as a limitation.

Outlet boundary conditions of these models employed a Windkessel approximation, representing local resistance and compliance with the downstream resistance, which have been shown to produce inaccuracies. In contrast, closed loop simulations have been initiated in recent years where the arterial, venous, and heart cavities (ventricles) are modeled, which would replicate more accurate hemodynamics for the coronary arteries. Recently the concept of multi-scale modeling, where representations of mechanical stimuli and biological function at a number of spatial and temporal scales are combined to provide a framework for examination of mechanobiology across the scales, suggests an alternative approach (Van Der Heiden et al., 2013).

Another limitation of this project is the uneven distribution of analyzed slices across stent types for cluster analysis. Due to the fact that the stents' lengths could range anywhere from 12mm to 38mm long in this research, a different number of analyzed slices for each stent type

were included in the cluster analysis. This disparity can be seen in the absolute distributions of the stent types in the left side of Figure 35, where the Nobori stent type is the most prevalent, followed by Promus and Xience. Ideally, there would be an even number of analyzed slices across all stent types to effectively compare the differences associated between the stents (i.e. geometry, drug-elution behavior, etc.).

The current findings suggesting an association between certain WSS indices and NT or resorption does not provide details on the potential molecular and cellular mediators of this process. Prior reports (Hierck et al., 2008; Koskinas, Chatzizisis, Antoniadis, & Giannoglou, 2012; Kraiss, Ennis, & Alto, 2001; Papafaklis et al., 2010) suggest the mechanisms of action for a DES may differentially impact the inverse relationship between NH and WSS previously observed with BMS, but this hypothesis remains to be tested.

One further limitation of the model creation process was that OCT images used in this study have 1mm increments along the length of the stented region, when the OCT system provides 0.1mm increments between images. Only the OCT images 1mm apart were provided for each case in this project. Though increasing the number of axial images to correspond with the patient-specific model would be far more time consuming, this increase in patient-specific data may allow for a better representation of the patients vessel geometry as well as deployed stent placement. However, adding twice as many OCT images to represent the stented region would, in turn, double the work done in the image processing steps of the model creation process and thereby prolong the time it takes to generate the CFD model.

A future direction of this research may involve a collective local cluster analysis of BVS. These devices are in their early stages of post-approval monitoring. They are not permanent like DES, and therefore theoretically allow the artery to recover from the initial stent deployment to a preferential baseline WSS value without a metal scaffold present.

Further validation of the documented results of this research would also be valuable, as this analysis is hypothesis driving, even more so for the recently proposed WSS indices.

In summary, the results of these cluster analyses showed the potential of post-stenting metrics and their predictive nature in the outcomes in stented coronary arteries. *Low TAWSS combined with high WSSET may be associated with restenosis, while high TAWSS combined with high TAWSS variability may be associated with positive remodeling, or resorption.* This collection of local analyses supported the predictive nature of these metrics due to the wide range of complex vessel geometries and various stent deployment patterns of the three DES platforms. Following additional prospective studies confirming these results, physicians may now be able to predict locations of potential concern in their patients with DES, and thereby improving the efficacy of current DES and improving the quality of life of patients with CAD.

BIBLIOGRAPHY

- Abbara, S., Arbab-Zadeh, A., Callister, T. Q., Desai, M. Y., Mamuya, W., Thomson, L., & Weigold, W. G. (2009). SCCT guidelines for performance of coronary computed tomographic angiography: A report of the Society of Cardiovascular Computed Tomography Guidelines Committee. *Journal of Cardiovascular Computed Tomography*, 3(3), 190–204. <https://doi.org/10.1016/j.jcct.2009.03.004>
- Alfonso, F., Byrne, R. A., Rivero, F., & Kastrati, A. (2014). Current treatment of in-stent restenosis. *Journal of the American College of Cardiology*, 63(24), 2659–2673. <https://doi.org/10.1016/j.jacc.2014.02.545>
- Antiga, L., & Steinman, D. A. (2014). Robust and Objective Decomposition and Mapping of Bifurcating Vessels, X(Xx), 1–11. Retrieved from <papers2://publication/uuid/DE63F07C-6F21-4E56-8BD5-5B023CC3C315>
- Arzani, A., Gambaruto, A. M., Chen, G., & Shadden, S. C. (2016a). Lagrangian wall shear stress structures and near-wall transport in high-Schmidt-number aneurysmal flows. *Journal of Fluid Mechanics*, 790, 158–172. <https://doi.org/10.1017/jfm.2016.6>
- Arzani, A., Gambaruto, A. M., Chen, G., & Shadden, S. C. (2016b). Wall shear stress exposure time: a Lagrangian measure of near-wall stagnation and concentration in cardiovascular flows. *Biomechanics and Modeling in Mechanobiology*, (November). <https://doi.org/10.1007/s10237-016-0853-7>
- Bittencourt, M. S., Hultén, E., Ghoshhajra, B., O’Leary, D., Christman, M. P., Montana, P., ... Blankstein, R. (2014). Prognostic Value of Nonobstructive and Obstructive Coronary Artery Disease Detected by Coronary Computed Tomography Angiography to Identify Cardiovascular Events. *Circulation-Cardiovascular Imaging*, 7(2), 282–291. <https://doi.org/10.1161/circimaging.113.001047>
- Bønaa, K. H., Mannsverk, J., Wiseth, R., Aaberge, L., Myreng, Y., Nygård, O., ... Nordrehaug, J. E. (2016). Drug-Eluting or Bare-Metal Stents for Coronary Artery Disease. *The New England Journal of Medicine*, 1–11. <https://doi.org/10.1056/NEJMoa1607991>
- Byrne, R. A., & Kastrati, A. (2015). Bioresorbable drug-eluting stents: An immature technology in need of mature application. *JACC: Cardiovascular Interventions*, 8(1), 198–200. <https://doi.org/10.1016/j.jcin.2014.11.010>
- Chiastra, C., Morlacchi, S., Gallo, D., Morbiducci, U., Cárdenes, R., Larrabide, I., & Migliavacca, F. (2013). Computational fluid dynamic simulations of image-based stented coronary bifurcation models. *Journal of the Royal Society, Interface / the Royal Society*, 10(84), 20130193. <https://doi.org/10.1098/rsif.2013.0193>

- Chiastra, C., Wu, W., Dickerhoff, B., Aleiou, A., Dubini, G., Otake, H., ... LaDisa, J. F. (2016). Computational replication of the patient-specific stenting procedure for coronary artery bifurcations: From OCT and CT imaging to structural and hemodynamics analyses. *Journal of Biomechanics*, *49*(11), 2102–2111. <https://doi.org/10.1016/j.jbiomech.2015.11.024>
- Chiu, T., Fang, D., Chen, J., Wang, Y., & Jeris, C. (2001). A Robust and Scalable Clustering Algorithm for Mixed Type Attributes in Large Database Environment, 263–268.
- Chopra, H. K., & Nanda, N. C. (2013). *Textbook of Cardiology: A Historical and Clinical Perspective*. Jaypee Brothers Medical Publishers LTD.
- Davies, P. F. (2009). Hemodynamic shear stress and the endothelium in cardiovascular pathophysiology. *Nat Clin Pract Cardiovasc Med*, *6*(1), 16–26. <https://doi.org/10.1038/ncpcardio1397>
- Dolan, J. M., Kolega, J., & Meng, H. (2013). High Wall Shear Stress and Spatial Gradients in Vascular Pathology: A Review. *Annals of Biomedical Engineering*, *41*(7), 1411–1427. <https://doi.org/10.1124/dmd.107.016501.CYP3A4-Mediated>
- Ellwein, L. M., Otake, H., Gundert, T. J., Koo, B. K., Shinke, T., Honda, Y., ... LaDisa, J. F. (2011). Optical Coherence Tomography for Patient-specific 3D Artery Reconstruction and Evaluation of Wall Shear Stress in a Left Circumflex Coronary Artery. *Cardiovascular Engineering and Technology*, *2*(3), 212–227. <https://doi.org/10.1007/s13239-011-0047-5>
- Gijsen, F. J. H., Oortman, R. M., Wentzel, J. J., Schuurbijs, J. C. H., Tanabe, K., Degertekin, M., ... Slager, C. J. (2003). Usefulness of shear stress pattern in predicting neointima distribution in sirolimus-eluting stents in coronary arteries. *American Journal of Cardiology*, *92*(11), 1325–1328. <https://doi.org/10.1016/j.amjcard.2003.08.017>
- Gow, B. S., & Hadfield, C. D. (1979). The elasticity of canine and human coronary arteries with reference to postmortem changes. *Circulation Research*, *45*(5), 588–594. <https://doi.org/10.1161/01.RES.45.5.588>
- Greenbaum, A., & Chartier, T. P. (2012). *Numerical Methods: Design, Analysis, and Computer Implementation of Algorithms*. Princeton University Press.
- Gundert, T. J., Dholakia, R. J., McMahon, D., & LaDisa Jr., J. F. (2013). Computational Fluid Dynamics Evaluation of Equivalency in Hemodynamic Alterations Between Driver, Integrity, and Similar Stents Implanted Into an Idealized Coronary Artery. *Journal of Medical Devices*, *7*(1), 11004. <https://doi.org/10.1115/1.4023413>

- Gundert, T. J., Marsden, A. L., Yang, W., Marks, D. S., & LaDisa, J. F. (2012). Identification of hemodynamically optimal coronary stent designs based on vessel caliber. *IEEE Transactions on Biomedical Engineering*, 59(7), 1992–2002. <https://doi.org/10.1109/TBME.2012.2196275>
- Gundert, T. J., Shadden, S. C., Williams, A. R., Koo, B. K., Feinstein, J. A., & Ladisa, J. F. (2011). A rapid and computationally inexpensive method to virtually implant current and next-generation stents into subject-specific computational fluid dynamics models. *Annals of Biomedical Engineering*, 39(5), 1423–1437. <https://doi.org/10.1007/s10439-010-0238-5>
- Guyton, A., & Hall, J. (2006). Textbook of medical physiology, 11th. In *Elsevier Saunders* (pp. 802–804). <https://doi.org/10.1093/jhered/est132>
- Hierck, B. P., Van Der Heiden, K., Alkemade, F. E., Van De Pas, S., Van Thienen, J. V., Groenendijk, B. C. W., ... Poelmann, R. E. (2008). Primary cilia sensitize endothelial cells for fluid shear stress. *Developmental Dynamics*, 237(3), 725–735. <https://doi.org/10.1002/dvdy.21472>
- Hughey, J. K. (2014). *Computational Evaluation of Shear Stress and Restenosis in Stented Coronary Arteries Using Optical Coherence Tomography*.
- Im, E., Kim, B. K., Ko, Y. G., Shin, D. H., Kim, J. S., Choi, D., ... Hong, M. K. (2014). Incidences, predictors, and clinical outcomes of acute and late stent malapposition detected by optical coherence tomography after drug-eluting stent implantation. *Circulation: Cardiovascular Interventions*, 7(1), 88–96. <https://doi.org/10.1161/CIRCINTERVENTIONS.113.000797>
- Komiyama, H., Takano, M., Hata, N., Seino, Y., Shimizu, W., & Mizuno, K. (2015). Neoatherosclerosis: Coronary stents seal atherosclerotic lesions but result in making a new problem of atherosclerosis. *World Journal of Cardiology*. <https://doi.org/10.4330/wjc.v7.i11.776>
- Koskinas, K. C., Chatzizisis, Y. S., Antoniadis, A. P., & Giannoglou, G. D. (2012). Role of endothelial shear stress in stent restenosis and thrombosis: Pathophysiologic mechanisms and implications for clinical translation. *Journal of the American College of Cardiology*, 59(15), 1337–1349. <https://doi.org/10.1016/j.jacc.2011.10.903>
- Kraiss, L. W., Ennis, T. M., & Alto, N. M. (2001). Flow-induced DNA synthesis requires signaling to a translational control pathway. *J Surg Res*, 97(1), 20–26. <https://doi.org/10.1006/jsre.2001.6091> [rS0022-4804(01)96091-3 [pii]]
- Kung, E. O. (2010). *In-vitro Experimental Validation of Finite Element Analysis of Blood Flow and Vessel Wall Dynamics*.

- Ladisa, J. F., Guler, I., Olson, L. E., Hettrick, D. A., Kersten, J. R., Warltier, D. C., & Pagel, P. S. (2003). Three-dimensional computational fluid dynamics modeling of alterations in coronary wall shear stress produced by stent implantation. *Annals of Biomedical Engineering*, 31(8), 972–980. <https://doi.org/10.1114/1.1588654>
- Ladisa, J. F., Olson, L. E., Guler, I., Hettrick, D. A., Kersten, J. R., Warltier, D. C., ... Pagel, P. S. (2005). Circumferential vascular deformation after stent implantation alters wall shear stress evaluated with time-dependent 3D computational fluid dynamics models, 53226, 947–957. <https://doi.org/10.1152/jappphysiol.00872.2004>.
- LaDisa, J. F., Olson, L. E., Guler, I., Hettrick, D. a, Audi, S. H., Kersten, J. R., ... Pagel, P. S. (2004). Stent design properties and deployment ratio influence indexes of wall shear stress: a three-dimensional computational fluid dynamics investigation within a normal artery. *Journal of Applied Physiology (Bethesda, Md. : 1985)*, 97(1), 424–430; discussion 416. <https://doi.org/10.1152/jappphysiol.01329.2003>
- LaDisa Jr., J. F., Hettrick, D. a, Olson, L. E., Guler, I., Gross, E. R., Kress, T. T., ... Pagel, P. S. (2002). Stent implantation alters coronary artery hemodynamics and wall shear stress during maximal vasodilation. *Journal of Applied Physiology (Bethesda, Md. : 1985)*, 93(6), 1939–1946. <https://doi.org/10.1152/jappphysiol.00544.2002>
- LaDisa Jr., J. F., Olson, L. E., Molthen, R. C., Hettrick, D. a, Pratt, P. F., Hardel, M. D., ... Pagel, P. S. (2005). Alterations in wall shear stress predict sites of neointimal hyperplasia after stent implantation in rabbit iliac arteries. *American Journal of Physiology. Heart and Circulatory Physiology*, 288(5), H2465–H2475. <https://doi.org/10.1152/ajpheart.01107.2004>
- Leaman, D. M., Brower, R. W., Meester, G. T., Serruys, P., & van den Brand, M. (1981). Coronary artery atherosclerosis: severity of the disease, severity of angina pectoris and compromised left ventricular function. *Circulation*, 63(2), 285–299. <https://doi.org/10.1161/01.CIR.63.2.285>
- Lee, S. Y., Hur, S. H., Lee, S. G., Kim, S. W., Shin, D. H., Kim, J. S., ... Hong, M. K. (2015). Optical coherence tomographic observation of in-stent neoatherosclerosis in lesions with more than 50% neointimal area stenosis after second-generation drug-eluting stent implantation. *Circulation: Cardiovascular Interventions*, 8(2), 1–10. <https://doi.org/10.1161/CIRCINTERVENTIONS.114.001878>
- Ma, B., Harbaugh, R. E., & Raghavan, M. L. (2004). Three-dimensional geometrical characterization of cerebral aneurysms. *Annals of Biomedical Engineering*, 32(2), 264–273. <https://doi.org/10.1023/B:ABME.0000012746.31343.92>
- Mahnken, A. H. (2012). CT Imaging of Coronary Stents : Past , Present , and Future, 2012. <https://doi.org/10.5402/2012/139823>

- Malek, A. M., & Alper, S. L. (2014). Hemodynamic Shear Stress and Its Role in Atherosclerosis, *282*(21), 2035–2042.
- Morlacchi, S., & Migliavacca, F. (2013). Modeling stented coronary arteries: Where we are, where to go. *Annals of Biomedical Engineering*, *41*(7), 1428–1444. <https://doi.org/10.1007/s10439-012-0681-6>
- Morris, P. D., Narracott, A., von Tengg-Kobligk, H., Silva Soto, D. A., Hsiao, S., Lungu, A., ... Gunn, J. P. (2015). Computational fluid dynamics modelling in cardiovascular medicine. *Heart (British Cardiac Society)*, heartjnl-2015-308044-. <https://doi.org/10.1136/heartjnl-2015-308044>
- Mozaffarian, D., Benjamin, E. J., Go, A. S., Arnett, D. K., Blaha, M. J., Cushman, M., ... Turner, M. B. (2016). Executive summary: Heart disease and stroke statistics-2016 update: A Report from the American Heart Association. *Circulation*, *133*(4), 447–454. <https://doi.org/10.1161/CIR.0000000000000366>
- Murphy, J., & Boyle, F. (2010). Predicting neointimal hyperplasia in stented arteries using time-dependant computational fluid dynamics: A review. *Computers in Biology and Medicine*, *40*(4), 408–418. <https://doi.org/10.1016/j.compbiomed.2010.02.005>
- Nakano, M., Otsuka, F., Yahagi, K., Sakakura, K., Kutys, R., Ladich, E. R., ... Virmani, R. (2013). Human autopsy study of drug-eluting stents restenosis: Histomorphological predictors and neointimal characteristics. *European Heart Journal*, *34*(42), 3304–3313. <https://doi.org/10.1093/eurheartj/eh241>
- Nichols, W. W., O'Rourke, M. F., & Vlachopoulos, C. (2011). *McDonald's Blood Flow in Arteries; Theoretical, Experimental and Clinical Principles. General Pharmacology: The Vascular System*. [https://doi.org/10.1016/0306-3623\(92\)90079-Y](https://doi.org/10.1016/0306-3623(92)90079-Y)
- Nordgaard, H., Swillens, A., Nordhaug, D., Kirkeby-Garstad, I., Van Loo, D., Vitale, N., ... Lovstakken, L. (2010). Impact of competitive flow on wall shear stress in coronary surgery: Computational fluid dynamics of a LIMA-LAD model. *Cardiovascular Research*, *88*(3), 512–519. <https://doi.org/10.1093/cvr/cvq210>
- Onuma, Y., Serruys, P. W., Perkins, L. E. L., Okamura, T., Gonzalo, N., García-García, H. M., ... Virmani, R. (2010). Intracoronary Optical Coherence Tomography and Histology at 1 Month and 2, 3, and 4 Years After Implantation of Everolimus-Eluting Bioresorbable Vascular Scaffolds in a Porcine Coronary Artery Model: An Attempt to Decipher the Human Optical Coherence Tomo. *Circulation*, *122*(22), 2288–2300. <https://doi.org/10.1161/CIRCULATIONAHA.109.921528>

- Papafaklis, M. I., Bourantas, C. V., Theodorakis, P. E., Katsouras, C. S., Naka, K. K., Fotiadis, D. I., & Michalis, L. K. (2010). The effect of shear stress on neointimal response following sirolimus- and paclitaxel-eluting stent implantation compared with bare-metal stents in humans. *JACC: Cardiovascular Interventions*, 3(11), 1181–1189. <https://doi.org/10.1016/j.jcin.2010.08.018>
- Parsa, E., Saroukhani, S., Majlessi, F., Poorhosseini, H., Lofti-Tokaldany, M., Jalali, A., ... Kassaian, S. E. (2016). Biodegradable-Polymer Biolimus-Eluting Stents versus Durable-Polymer Everolimus-Eluting Stents at One-Year Follow-Up: A Registry-Based Cohort Study. *Texas Heart Institute Journal*, 43(2), 126–130.
- Peiffer, V., Sherwin, S. J., & Weinberg, P. D. (2013). Does low and oscillatory wall shear stress correlate spatially with early atherosclerosis? A systematic review. *Cardiovascular Research*, 99(2), 242–250. <https://doi.org/10.1093/cvr/cvt044>
- Sarstedt, M., & Mooi, E. (2014). *A Concise Guide to Market Research: The Process, Data and Methods Using IBM SPSS Statistics. Springer Texts in Business and Economics*. <https://doi.org/10.1007/978-3-642-12541-6>
- Seo, T., Lafont, A., Choi, S. Y., & Barakat, A. I. (2016). Drug-Eluting Stent Design is a Determinant of Drug Concentration at the Endothelial Cell Surface. *Annals of Biomedical Engineering*, 44(2), 302–314. <https://doi.org/10.1007/s10439-015-1531-0>
- SJM. (n.d.). No Title. Retrieved from [http://www.terapeuticasintervencionistas.com/instrumental/C7 Dragonfly Intravascular Imaging Cathter Intl.pdf](http://www.terapeuticasintervencionistas.com/instrumental/C7%20Dragonfly%20Intravascular%20Imaging%20Cathter%20Intl.pdf)
- Stefanini, G. G., & Holmes, D. R. (2013). Drug-Eluting Coronary-Artery Stents. *New England Journal of Medicine*, 368, 254–65. <https://doi.org/10.1056/NEJMra1210816>
- Stergiopoulos, N., Segers, P., & Westerhof, N. (1999). Use of pulse pressure method for estimating total arterial compliance in vivo. *The American Journal of Physiology*, 276(2 Pt 2), H424–H428.
- Stettler, C., Wandel, S., Allemann, S., Kastrati, A., Morice, M. C., Schömig, A., ... Jüni, P. (2007). Outcomes associated with drug-eluting and bare-metal stents: a collaborative network meta-analysis. *Lancet*, 370(9591), 937–948. [https://doi.org/10.1016/S0140-6736\(07\)61444-5](https://doi.org/10.1016/S0140-6736(07)61444-5)
- Suzuki, N., Nanda, H., Angiolillo, D. J., Bezerra, H., Sabaté, M., Jiménez-Quevedo, P., ... Costa, M. a. (2008). Assessment of potential relationship between wall shear stress and arterial wall response after bare metal stent and sirolimus-eluting stent implantation in patients with diabetes mellitus. *The International Journal of Cardiovascular Imaging*, 24(4), 357–64. <https://doi.org/10.1007/s10554-007-9274-0>

- Van Der Heiden, K., Gijzen, F. J. H., Narracott, A., Hsiao, S., Halliday, I., Gunn, J., ... Evans, P. C. (2013). The effects of stenting on shear stress: Relevance to endothelial injury and repair. *Cardiovascular Research*, 99(2), 269–275. <https://doi.org/10.1093/cvr/cvt090>
- Van Huis, G. a, Sipkema, P., & Westerhof, N. (1987). Coronary input impedance during cardiac cycle as determined by impulse response method. *The American Journal of Physiology*, 253(2 Pt 2), H317-24. Retrieved from <http://www.ncbi.nlm.nih.gov/pubmed/3618806>
- Vergallo, R., Papafaklis, M. I., Yonetsu, T., Bourantas, C. V., Andreou, I., Wang, Z., ... Jang, I. K. (2014). Endothelial shear stress and coronary plaque characteristics in humans combined frequency-domain optical coherence tomography and computational fluid dynamics study. *Circulation: Cardiovascular Imaging*, 7(6), 905–911. <https://doi.org/10.1161/CIRCIMAGING.114.001932>
- Wayangankar, S. A., & Ellis, S. G. (2015). Bioresorbable Stents: Is This Where We Are Headed? *Progress in Cardiovascular Diseases*, 58(3), 342–355. <https://doi.org/10.1016/j.pcad.2015.08.011>
- Westerhof, N. (2010). *Snapshots of Hemodynamics: An Aid for Clinical Research and Graduate Education*. *Snapshots of Hemodynamics: An Aid for Clinical Research and Graduate Education*. <https://doi.org/10.1007/978-1-4419-6363-5>
- Williams, A. R., Koo, B. K., Gundert, T. J., Fitzgerald, P. J., & LaDisa, J. F. (2010). Local hemodynamic changes caused by main branch stent implantation and subsequent virtual side branch balloon angioplasty in a representative coronary bifurcation. *Journal of Applied Physiology (Bethesda, Md. : 1985)*, 109(2), 532–540. <https://doi.org/10.1152/jappphysiol.00086.2010>